

Dark dust II: Properties in the general field of the diffuse ISM

R. Siebenmorgen

European Southern Observatory, Karl-Schwarzschild-Str. 2, D-85748 Garching b. München, Germany; email: Ralf.Siebenmorgen@eso.org

Received April 25, 2022 / Accepted xxx, xxx

ABSTRACT

Distance estimates derived from spectroscopy or parallax have been unified by considering extinction by large grains. The addition of such a population of what is called *dark dust* to models of the diffuse interstellar medium is tested against a contemporary set of observational constraints. The dark dust model explains, by respecting representative solid-phase element abundances, simultaneously the typical wavelength-dependent reddening, extinction, and emission of polarized and unpolarized light by interstellar dust particles between far UV and millimetre wavelengths. The physical properties of dark dust are derived. Dark dust consists of micrometre-sized particles, which have been recently detected in-situ. It provides significant wavelength-independent reddening from the far UV to the near infrared. Light absorbed by dark dust is re-emitted in the submillimeter region by grains at dust temperatures of 8 – 12 K. Such very cold dust has been frequently observed in external galaxies. Dark dust contributes to the polarisation at $\gtrsim 1$ mm to $\sim 35\%$ and at shorter wavelengths marginally. Optical constants for silicate dust analogous are investigated. By mixing 3% in mass of $\text{Mg}_{0.8}\text{Fe}_{0.2}^{2+}\text{SiO}_3$ to $\text{MgO}-0.5\text{SiO}_2$ a good fit to the data is derived that still can accommodate up to 5 - 10% of mass in dark dust. The extra dimming of light by dark dust is unexplored when discussing SN Ia light curves and in other research. Previous models that ignore dark dust do not account for the unification of the distance scales.

Key words. (ISM:) dust, extinction, Polarization, (ISM:) Infrared: ISM, Stars: distances

1. Introduction

Physical properties of dust in the diffuse interstellar medium (ISM) are derived by confronting models against observational constraints. Two classes of models emerged over the years, either those that employ distinct grain populations (Mathis et al. 1977; Draine & Lee 1984; Desert et al. 1990; Weingartner & Draine 2001; Zubko et al. 2004; Compiegne et al. 2011; Siebenmorgen et al. 2014) or models which are using a mixture of different grain constituents forming composite particles (Hage & Greenberg 1990; Mathis & Whiffen 1989; Ossenkopf 1991; Krügel & Siebenmorgen 1994; Greenberg et al. 1995; Voshchinnikov 2012; Jones et al. 2013; Siebenmorgen et al. 2014; Köhler et al. 2015; Ysard et al. 2015; Jones et al. 2017; Guillet et al. 2018; Draine & Hensley 2021a). The present observational status of ISM dust characteristics after the Planck mission (Planck Collaboration et al. 2014) has been reviewed by Hensley & Draine (2021). Dust models shall agree with several major observations:

- a) The solid-phase element abundances in the medium out of which the dust is made (Hensley & Draine 2021).
- b) The reddening curves in the Milky Way (Fitzpatrick & Massa 2007; Gordon et al. 2009; Fitzpatrick et al. 2019).
- c) The diffuse galactic dust emission that has been observed in the wavelength range from a few μm up to several mm by space missions ISO, AKARI, Spitzer, WMAP, DIRBE (Dwek et al. 1997), and Planck (Planck Collaboration et al. 2014).
- d) The optical/near-infrared (NIR) starlight polarization (Serkowski et al. 1975), which is due to the dichroic extinction of aligned non-spherical dust particles (Hong & Greenberg 1980; Krügel 2008; Draine & Fraise 2009; Siebenmorgen et al. 2014; Voshchinnikov 2012).
- e) The polarized emission spectrum of the same grains which is predominantly observed by Planck Collaboration et al. (2020).

Strikingly previous dust models in the pre-Planck era systematically under-predict the observed submillimeter (submm) and mm emission of unpolarized light from about 0.3–3 mm, and did not explain the flatness of the polarized dust emission spectrum in that wavelength range.

f) In addition, the unification of spectroscopically derived distances with the parallax is not closed.

However, previous dust models failed to explain all observational constraints that have been available in the post-Planck era simultaneously (Ysard 2020), unless the model by Draine & Hensley (2021a), in which the optical constants of amorphous silicates were modified to fit the Planck data.

For a star the spectro-photometric distance D_{SpL} shall agree with the distance D_{GAIA} derived from parallax. Geometric distances using GAIA (Gaia Collaboration et al. 2016) as derived by Bailer-Jones et al. (2018, 2021) show for OB stars with available reddening curves at distances below 2 kpc a fractional error of $\sim 5\%$. The photometric distance of a star is connected via the apparent m_V and absolute magnitude M_V , and the dust extinction A_V along that sightline: $\log D_{\text{SpL}} = 0.2(m_V - M_V - A_V + 5)$ pc. Photometric distances require accurate calibration of the spectral type and luminosity class (SpL) of the star allowing derivation of M_V and A_V (Eq.4). The original SpL estimates of OB stars (Walborn 1971; Walborn & Fitzpatrick 1990) have gained significantly in precision using results of the galactic O star spectroscopic survey (Maíz-Apellániz et al. 2004) with SpL updates by Sota et al. (2011, 2014) and applying quantitative spectral classification schemes utilizing high-resolution optical spectroscopy (Markova et al. 2011; Martins 2018). Standard grids of absolute magnitudes for OB stars are provided (Bowen et al. 2008; Pecaut & Mamajek 2013)¹ as well as high-quality extinction estimates

¹ <http://www.pas.rochester.edu/~mamajek/>

(Maíz Apellániz & Barbá 2018). This progress enables computing spectro-photometric distances of OB stars at fractional precision of $\sim 15\%$ for the nearby (2 kpc) sample. Photometric versus parallax distance estimates to galactic OB stars have been discussed by Shull & Danforth (2019) and reveal larger uncertainties at larger distances. In the nearby sample, the spectroscopic distances show a systematic overestimate with a dispersion above these errors (Siebenmorgen et al. 2020). Both distance estimates of the same source shall of course agree.

Already Trumpler (1930) included in the original form of the photometric equation, in addition to the wavelength-dependent (selective) interstellar extinction, a constant, wavelength-independent (non-selective) extinction component in the optical. He proposed that light may be obscured by large ('meteoritic') particles. Large micrometre-sized dust particles are frequently found in circumstellar shells (Strom et al. 1971; Jones 1972; Lanz et al. 1995; Steinacker et al. 2015; Kataoka et al. 2017), Herbig stars (Dunkin & Crawford 1998), η Car (Andriess et al. 1978) and other evolved stars (Scicluna et al. 2015, 2022). Grains larger than $2\mu\text{m}$ have been seen in scattering light halos around X-ray sources (Witt et al. 2001) and grains as large as $\sim 4\mu\text{m}$ have been suggested for V404 Cygni by Heinz et al. (2016). The emission from $100\mu\text{m}$ large particles accounting for the observed submm fluxes from evolved giants are derived by Jura et al. (2001). Maercker et al. (2022) finds that for carbon stars preferentially $\sim 2\mu\text{m}$ sized grains survive the AGB wind-ISM interaction regions and act later as seeds for grain growth in the ISM.

Distance estimates of the Orion Trapezium star HD 37020 using spectral type-luminosity distance D_{SpL} are a factor 2.5 larger than the Ca II or VLBI parallax distance estimates (Krełowski et al. 2016). For several nearby ($\lesssim 400\text{ pc}$) OB stars a significant overestimate of the spectroscopic distance over the HIPPARCOS parallax is reported by Skórzyński et al. (2003). Assuming that the parallax has been correctly measured the derived absolute magnitudes of these stars appear too faint. "Super large" grains are suggested for the extra weakening of the observed brightness of these stars. The column density of this very large grain population is well correlated with the strength of DIB 6367 Å and DIB 6425 Å and therefore appears distributed along the sightline through the diffuse ISM. The spectral type-luminosity distances of 132 OB stars have been compared to those derived by GAIA up to $D_{\text{GAIA}} < 2\text{ kpc}$ (Siebenmorgen et al. 2020) and for $\sim 10\%$ of the sample $D_{\text{SpL}}/D_{\text{GAIA}} \gtrsim 2$. Both distance estimates have been unified introducing $0.3 - 0.7\text{ mag}$ reddening by what they called *dark dust*. The terminology follows the unveiling of *dark gas* by Grenier et al. (2005) because gas and dust are intimately mixed in the diffuse ISM. It describes a mysterious, dimmed and hidden nebulousity. Extensive clouds of dark gas have been weighted using Fermi-LAT γ -ray data by Widmark et al. (2022) and emerge in the cold ISM. The hidden dust component appears in sightlines that are connected to the cold ISM as well and have line intensity ratio of CH 4300 Å to CH⁺ 4233 Å greater than one and CN 3875 Å detected. Possibly a sticking of smaller grains into larger units is favoured in cold ISM environments. A circumstellar nature of dark dust towards these stars is excluded from inspecting WISE imaging between $3 - 22\mu\text{m}$. Micrometre-sized particles from the diffuse ISM have been measured *in-situ* from the Ulysses, Galileo, and Stardust space probes to the outer solar system (Landgraf et al. 2000; Westphal et al. 2014; Krüger et al. 2015).

The emission of dark dust as a new component of the diffuse ISM should be observable in the submm/mm wavelength

range. It will absorb a fraction of the interstellar radiation field, ISRF (Mathis et al. 1983). As such grains are big they are cold and will emit at long wavelengths. Originally very cold ($\lesssim 15\text{ K}$) dust emission has been detected in the general field of the ISM of non-active galaxies (Krügel et al. 1998; Siebenmorgen et al. 1999) and in our Galaxy towards high-density regions (Chini et al. 1993). More recently, the Herschel KINGFISH (Kennicutt et al. 2011) and Dwarf Galaxy (Madden et al. 2013) surveys find that 35 out of 78 galaxies have excess emission at 0.5 mm that cannot be explained by a single modified black-body temperature component with dust emissivity spectral index of two (Rémy-Ruyer et al. 2013a). Other galaxies, e.g. Haro 11 (Galliano et al. 2005; Galametz et al. 2009), show the excess emission at even longer wavelengths in the mm range and were missed by Herschel surveys. The excess emission is due to very cold dust at temperatures as low as 10 K . A solution for explaining the submm excess emission is often favoured by ad-hoc adjustments of the emissivity law of the grains (Rémy-Ruyer et al. 2013b; Guillet et al. 2018). This can be derived by changes in the porosity, shape, or adjustments of the optical constants (Draine & Hensley 2021a). Models changing the spectral index of the dust emissivity do not touch on the issue of distance unification.

In this paper, a model for the general field in the diffuse ISM is described that accounts simultaneously for observations of solid-phase elemental abundances, average Milky Way reddening, IR to mm emission at high galactic latitudes, average Milky Way polarized extinction and polarized emission by dust. A particular feature is the inclusion of dark dust as an additional dust population that accounts for the very cold emission that is detected in the submm/mm range. Dark dust may solve the puzzle between discrepant spectroscopic and parallax-derived distance estimates. First, the observational basis is specified, then the dust model is described, and a vectorized fitting procedure of the 11-parameter dust model to the observational constraints is detailed. Results will be presented that show the overall success of the model in fitting the data and deriving the physical properties of dark dust. Particular attention is given to the use of optical constants of amorphous silicates (Demayk et al. 2022). The main findings are summarized in the conclusions.

2. Observations

2.1. Solid-phase abundances

Depletion of elements from the gas into dust is estimated by Voshchinnikov & Henning (2010) as the difference between abundances in the Sun (Asplund et al. 2009) and that of the gas (Jenkins 2009). Elemental depletion is used to infer dust compositions and some form of grains with silicate and carbon is widely accepted. Abundances of element [X] to that of hydrogen [H] are summarized by Hensley & Draine (2021) for the gas and the dust phase, respectively. The most abundant elements in dust are: O (249 ± 94), C (126 ± 56), Mg (46 ± 5), Fe (43 ± 4), Si (38 ± 3), S (7.6), Al (3.4), Ca (3.2), and Ni (2.0), where numbers in parenthesis give [X]/[H] (ppm). An over-abundance of O in the dust is noted and upper limits of the $16\mu\text{m}$ and $22\mu\text{m}$ bands of iron-oxides indicate that most of the Fe remain unexplained as well (Draine & Hensley 2021a). However, the Fe abundance is insufficient to form large grains (Zhukovska et al. 2018). Fe particles heated by the ISRF contribute to the emission at $\sim 60\mu\text{m}$ (Fischera 2004). Draine & Hensley (2021a) showed that the absorption cross-section remains in the IR - mm unaltered when including the available Fe in form of impurities in large particles.

Dust abundances are uncertain and estimates of the C and Si abundance in dust scatter by 50%. Mulas et al. (2013) find an average of $[C]/[H] = 145$ ppm. The Si abundance in the dust is estimated by Sofia & Meyer (2001) to be 18 ± 9 ppm, while Nieva & Przybilla (2012) derive 32 ± 3 ppm. Voshchinnikov & Henning (2010) find a sharp difference in the dust abundances for sightlines located at low and high galactic latitudes and give an average abundance of $[Si]/[H] = 23 \pm 5$ ppm.

Absorption and emission signatures of the dust provide important constraints on the composition. A striking feature is the 2175 Å extinction bump, where graphite and polycyclic aromatic hydrocarbons (PAHs; Allamandola et al. (1989)) have strong electronic transitions. In the IR, there are conspicuous emission bands at 3.3, 6.2, 7.7, 8.6, 11.3, and 12.7 μm, as well as a wealth of weaker bands in the 12 – 24 μm region. These bands are ascribed to vibrational transitions in PAH molecules, which are planar structures that consist of benzol rings with hydrogen attached. PAH feature strengths depend on the hardness of the exciting radiation field and the ionisation or hydrogenation coverage of the molecules.

Absorption features in the diffuse ISM between 3 – 8 μm are interpreted as being due to either carbonaceous material (Mennella et al. 2003) or, guided by laboratory spectra, by ices mixed with silicates (Potapov et al. 2021). Dust models including interstellar ice mixtures have been presented by Siebenmorgen & Gredel (1997). Solid-state water mixed with silicates would explain a good fraction of the unaccounted oxygen depletion in the diffuse ISM (Potapov et al. 2021). A comparison of future JWST observations against laboratory spectra is needed to confirm the existence of solid water in the diffuse ISM. Ices are not further considered in this study.

The 9.7 μm and 18 μm broadband features are assigned to Si-O stretching and O-Si-O bending modes of silicate grains, respectively. A comparison of the observed band profiles and laboratory spectra favours amorphous rather than crystalline silicates. Intriguing is the detection of the 11.1 μm absorption band that is attributed in the atlas of ground-based mid-infrared (MIR) spectra by Do-Duy et al. (2020) to forsterite, providing a mass abundance of crystalline silicates of ~ 2% in the diffuse ISM. Olivine ($Mg_{2x}Fe_{2-2x}SiO_4$ has $x \sim 0.8$), have been detected in AGB and T Tauri stars, and comet Hale-Bopp (Henning 2010). The silicate stoichiometry and grain geometry can be revealed by MIR spectro-polarimetry (Sec. 2.4). As nominal composition Draine & Hensley (2021a) adopt $Mg_{1.3}(Fe,Ni)_{0.3}SiO_{3.6}$ having a molecular weight of $\mu = 134.5$. In that structure, the silicate grain abundance is limited by Mg with a dust abundance ratio $[C]/[Si] \sim [C] 1.3/[Mg] \sim 3.5$. To accommodate the reported large scatter of ~ 50 % in the solid-phase element abundances the dust models shall respect a limit of the dust abundance ratio of

$$[C]/[Si] \lesssim 5.25. \quad (1)$$

2.2. Reddening and extinction

The interstellar reddening is derived by measuring the flux ratio of a reddened and unreddened star with the same SpL luminosity class, e.g. the standard pair method (Stecher 1965). The flux of a star is derived from the spectral luminosity $L(\lambda)$, the distance D , and the extinction optical depth $\tau(\lambda)$, which is due to the ab-

sorption and scattering of photons along the sightline excluding emission. The observed flux of the reddened star is given by

$$F(\lambda) = \frac{L(\lambda)}{4\pi D^2} e^{-\tau(\lambda)}. \quad (2)$$

In photometry it is customary to express the flux of an object by the apparent magnitude, which is related to the flux through $m(\lambda) = 2.5 \log_{10}(F(\lambda)/w_\lambda)$ and w_λ as the zero point of the photometric system. The difference in magnitudes between two stars is $\Delta m(\lambda) = 1.086 \times (\tau(\lambda) + 2 \log_{10}(D/D_0))$. Unfortunately, distances to hot, early-type stars, commonly used to measure interstellar extinction, are often subject to large errors (Siebenmorgen et al. 2020). Hence one relies on relative measurements of two wavelengths and defines the colour excess $E(\lambda - \lambda') = \Delta m(\lambda) - \Delta m(\lambda')$. The *reddening curve* $E(\lambda)$ is traditionally represented by a colour excess and normalisation to avoid the uncertainties between both distances,

$$E(\lambda) = \frac{E(\lambda - V)}{E(B - V)} = \frac{A_\lambda - A_V}{A_B - A_V} = \frac{\tau_\lambda - \tau_V}{\tau_B - \tau_V}. \quad (3)$$

Naturally, for the V and B band, $E(V) = 0$ and $E(B) = 1$. The extinction in magnitudes at wavelength λ is denoted by $A(\lambda)$. One obtains some extrapolated estimate of the visual extinction A_V from photometry. This requires measuring $E(B - V)$ and extrapolating the reddening curve to infinite wavelengths $E(\infty)$. In practice, one derives $E(\lambda - V)$ at the longest wavelength, which is not contaminated by any kind of emission. From this wavelength, e.g. the H-band, one extrapolates to infinite wavelengths assuming some prior shape of $E(\lambda)$ and hence estimates $E(\infty, V)$. By introducing the ratio of the *total-to-selective extinction*

$$R_V = \frac{A_V}{E(B - V)}, \quad (4)$$

where obviously $E(\infty) = -R_V$. The total-to-selective extinction can also be written using Eq. 3 or applying a dust model as

$$R_V = \frac{\tau_V}{\tau_B - \tau_V} = \frac{K_V}{K_B - K_V}, \quad (5)$$

where $K = K_{abs} + K_{sca}$ is the extinction cross-section which is the sum of the total absorption and scattering cross-section of the dust. The relation between reddening and extinction is

$$\frac{\tau(\lambda)}{\tau_V} = \frac{K(\lambda)}{K_V} = \frac{E(\lambda)}{R_V} + 1, \quad (6)$$

The International Ultraviolet Explorer (IUE) operated between 0.185 – 0.33 μm and the Far Ultraviolet Spectroscopic Explorer (FUSE) observed between 0.119 – 0.905 μm. IUE and FUSE provide the legacy of (far) UV spectra with a total of 895 reddening curves towards more than 568 early-type (OB) stars (Valencic et al. 2004; Fitzpatrick & Massa 2007; Gordon et al. 2009). The database of available reddening curves was scrutinized against systematic errors by the following means: 1) IUE/FUSE spectra were verified to include only a single star in the observing aperture and not beside the program star and other almost equally bright objects. 2) Although most early-type stars are binaries (Chini et al. 2012) their reddening curves are generally derived assuming a single star. Whenever the companion contributes significantly to the total flux of the system, the

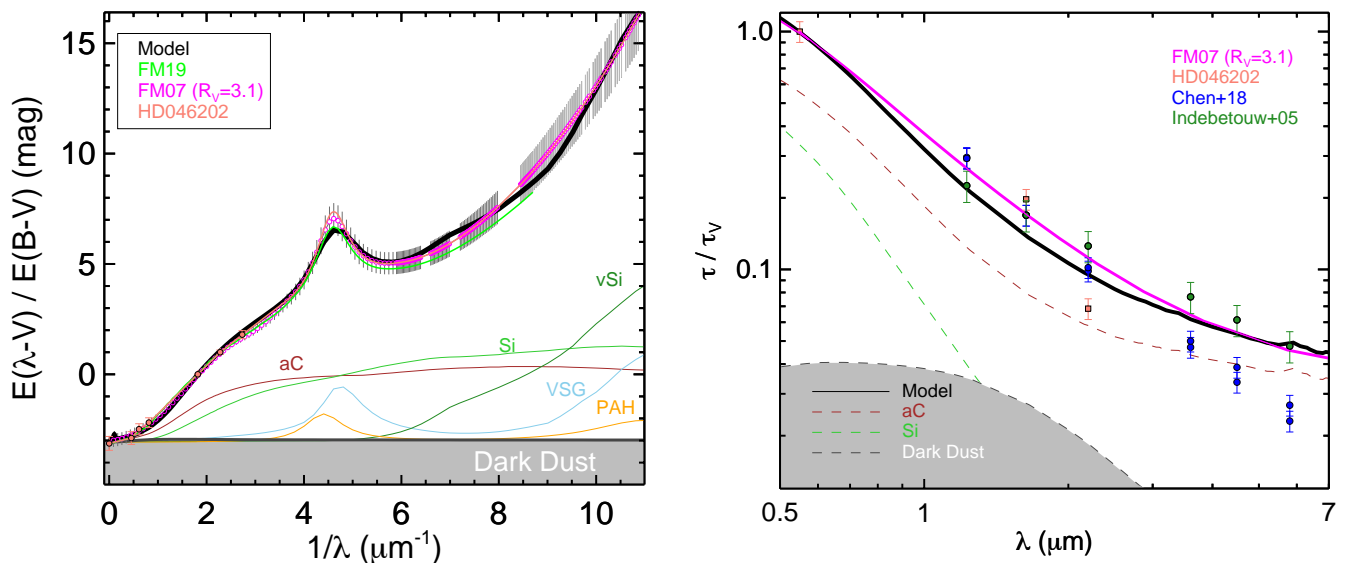


Fig. 1. Reddening (left) and extinction (right) of the diffuse ISM (Fitzpatrick & Massa 2007; Fitzpatrick et al. 2019; Indebetouw et al. 2005; Chen et al. 2018) and of HD 046202 (Gordon et al. 2009). Model (black) with $r_{\text{Dark}}^+ = 1 \mu\text{m}$ (Table 1) and individual dust components as labelled. The area in grey shows the contribution of dark dust.

derived extinction includes large systematic errors. 3) A large fraction of the OB stars show emission components above the photosphere in the IR (Siebenmorgen et al. 2018a; Deng et al. 2022), which prohibits deriving meaningful reddening in the IR. 4) Reddening curves are derived assuming steady stellar systems. Stellar variability will thus systematically impact the derived reddening. Stars with detected variability between ground-based and Hipparcos V-band photometry ($\gtrsim 0.1$ mag), significant B - V colour changes, or GAIA G-band photometry of more than ($\gtrsim 0.033$ mag) shall be rejected. 5) some stars show inconsistencies in the GAIA parallaxes between data release two (Gaia Collaboration et al. 2018) and data release three (Gaia Collaboration et al. 2020) that are not instrumental so that their reddening curves shall be declared as spurious. 6) Finally, the quality of the derived reddening curve depends critically on the fidelity of the SpL estimate. The SpL determination of fast rotators is highly uncertain and UV spectral diagnostics indicate considerably earlier SpL (hotter) classifications than optically assigned SpL. Reddening curves with largely deviating SpL assignments shall be ignored. All these systematic effects impact the derivation more dramatic at $\lambda \gtrsim 1 \mu\text{m}$ and the extinction more than the reddening. In total, 48 stars with one or more reddening curves passing the rejection criteria are available with 21 classified as multi-component sightlines and 27 as single-cloud sightlines (Siebenmorgen et al. 2020). The reddening curves in the ISM show significant variations from sightline-to-sightline and the derived total-to-selective extinction are between $2 \lesssim R_V \lesssim 6.4$. For the same star the published R_V that are mostly extrapolated from JHK photometry, scatter typically by 10%. Even in the high-quality sample, the peak-to-peak scatter in R_V estimates of the same star are up to ± 0.6 . The scatter might be reduced by detailed physical modelling of the dust applying Eq. (5). Whenever possible the reddening instead of the extinction curve shall be discussed.

For the diffuse ISM a mean reddening of $E(B-V) = 0.45$ mag and a median and mean value of $R_V = 3.22$ and 2.99 ± 0.27 is derived by Fitzpatrick & Massa (2007), respectively; Wang & Chen (2019) find $R_V = 3.16$, and Voshchinnikov (2004); Fitzpatrick et al. (2019) give $A_V \sim 3.1 E(B-V)$. Here $R_V = 3.1$ is adopted as by Hensley & Draine (2021). The mean reddening curve of the Milky Way is derived for $1/\lambda \lesssim 1./8 \mu\text{m}$ by Fitzpatrick & Massa (2007) and Fitzpatrick et al. (2019) and both are shown together with the reddening curve of HD 046202 (Gordon et al. 2009) in Fig. 1. The reddening curve of that star perfectly matches the mean curve derived from IUE and FUSE. Reddening in spectral regions close to wind lines at 6.5 and $7.1 \mu\text{m}^{-1}$ and Ly- α at $8 \mu\text{m}^{-1} \leq x \leq 8.45 \mu\text{m}^{-1}$, or with apparent instrumental noise at $x \lesssim 3.6 \mu\text{m}^{-1}$ shall be ignored. Overall a typical error in the derived reddening is $\sim 10\%$. Various mean extinction curves of the diffuse ISM between $0.5 - 7 \mu\text{m}$ are also shown in Fig. 1. Noticeable is the large scatter which is increasing towards longer wavelengths.

2.3. Diffuse galactic dust emission

Diffuse emission of the ISM from dust grains heated by the ambient ISRF has been observed from the NIR through the microwave region. The dust emission of the diffuse ISM is not uniform across the sky and there is evidence that the properties of the dust as well as the spectral distribution and strength of the ISRF that heats the dust vary (Fanciullo et al. 2015). Observations of this component for high galactic latitude ($|b| \gtrsim 25^\circ$) from the Cosmic Background Explorer using DIRBE data are given by Dwek et al. (1997) and from the Planck Collaboration et al. (2015). A colour-corrected composite spectrum with error estimates is tabulated by Hensley & Draine (2021). The emission spectrum is shown in Fig. 2.

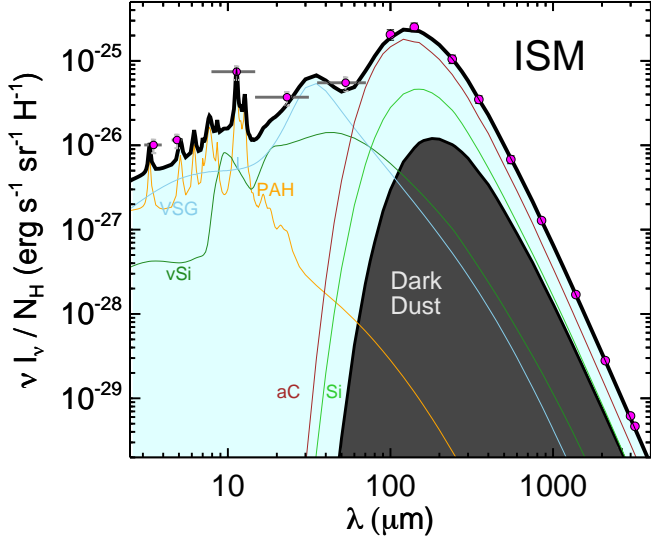


Fig. 2. Dust emission of the diffuse ISM observed at high galactic latitudes and normalised per H atom by Dwek et al. (1997) and Planck Collaboration et al. (2015) and as tabulated by Hensley & Draine (2021). Model (black) with $r_{\text{Dark}}^+ = 1 \mu\text{m}$ (Table 1) and individual dust components as labelled. The area in grey shows the contribution of dark dust.

2.4. Starlight and FIR polarization

Stellar light that passes a cloud of moderate extinction by aligned grains becomes linearly polarized. From the far UV to the NIR, between $0.12 \mu\text{m} - 1.6 \mu\text{m}$, the polarization curves are fit by an empirical formula given by Serkowski et al. (1975)

$$p(\lambda) = p_{\text{max}} \exp \left[-k_p \ln^2 \left(\frac{\lambda_{\text{max}}}{\lambda} \right) \right]. \quad (7)$$

where λ_{max} is the wavelength at maximum polarization p_{max} and k_p the width of the spectrum. Significant variations in the width $0.5 \leq k_p \leq 1.5$ towards different sightlines are observed, using HPOL², the Wisconsin UV Photo-Polarimeter WUPPE satellites, and ground-based instruments as compiled by Efimov (2009) and by the Large Interstellar Polarization Survey (Bagnulo et al. 2017). The latter authors could not confirm the linear trend of $k_p \propto \lambda_{\text{max}}$ claimed in earlier work (Willing et al. 1980; Whittet et al. 1992). Observations of 160 sightlines of mildly reddened stars show that $p_V/E_{B-V} \lesssim 9 \text{ \%}/\text{mag}$ and $p_{\text{max}} \lesssim 10 \text{ \%}$ (Voshchinnikov et al. 2016). Starlight polarization reaches a maximum in the V band at $\lambda_{\text{max}} = 0.545 \mu\text{m}$ and $k_p = 1.15$ is selected to represent the mean Serkowski curve that shows a typical scatter of 5% near p_{max} , 10% at $p/p_{\text{max}} \lesssim 0.4$, and in the NIR $\sim 15 \text{ \%}$. At $\lambda > 1.5 \mu\text{m}$ the polarization spectrum smoothly matches onto a power-law with an exponent of 1.6 (Martin et al. 1992). The fit naturally breaks in the MIR near the silicate band. The typical wavelength dependence of the observed polarized extinction is shown in the optical/NIR in Fig. 3 and in the MIR in Fig. 4.

A mean MIR polarized extinction spectrum, which covers the silicate band, is constructed by Wright et al. (2002) by averaging observations of two Wolf-Rayet stars, WR 48A and AFGL 2104. The analysis by Wright shows that the polarized extinction of silicates with stoichiometry and optical constants

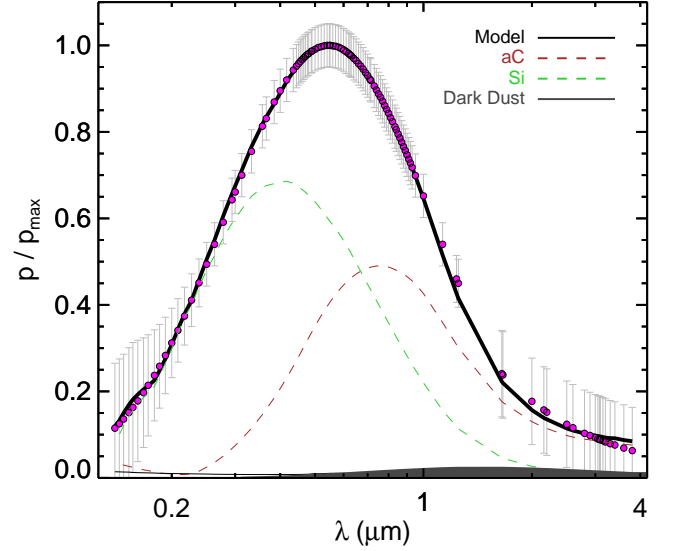


Fig. 3. Polarized extinction of the diffuse ISM (circles) with error bars indicating the observed scatter (Voshchinnikov et al. 2012; Bagnulo et al. 2017). The model (black) with $r_{\text{Dark}}^+ = 1 \mu\text{m}$ (Table 1) and contributions (dashed) from large amorphous carbon (brown), large silicate grains (green), and dark dust area in grey, when treated as prolate particles, is shown.

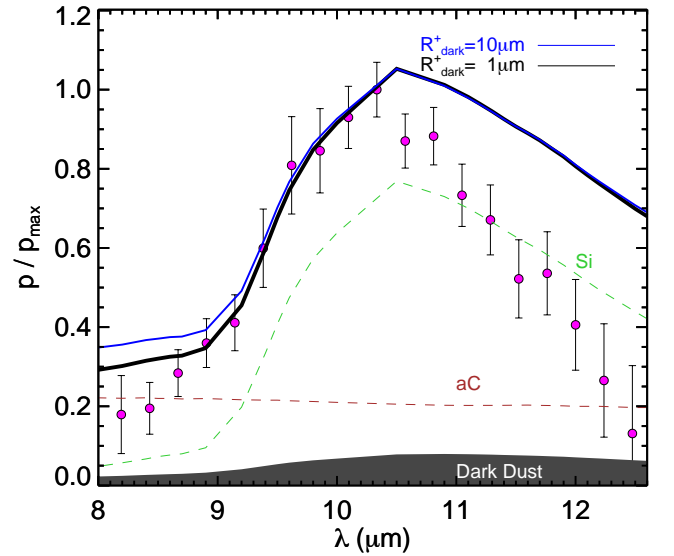


Fig. 4. Polarized extinction in the MIR. A composite spectrum (circles) of two Wolf-Rayet stars WR 48A and AFGL 2104 by Wright et al. (2002), the model (full line) with $r_{\text{Dark}}^+ = 1 \mu\text{m}$ (black) and contribution (dashed) from large amorphous carbon (brown), large silicate grains (green), and dark dust (grey) when treated as prolate particles, is shown, as well as the model with $r_{\text{Dark}}^+ = 10 \mu\text{m}$ (blue). Parameters as in Table 1.

(n, k) of $\text{Mg}_{0.4}\text{Fe}_{0.6}\text{SiO}_3$, MgFeSiO_3 , as well as MgFeSiO_4 provide a pure fit whereas $\text{Mg}_{0.8}\text{Fe}_{1.2}\text{SiO}_4$ give an almost perfect fit to the polarization spectrum (Wright et al. 2002). The molecular weight of these materials varies between $\mu = 97 - 141$, an uncertainty directly impacting estimates of the gas-to-dust mass

² <http://www.sal.wisc.edu>

ratio. The silicate composition observed towards the Wolf-Rayet stars is distinct from $\text{Mg}_{1.3}(\text{Fe},\text{Ni})_{0.3}\text{SiO}_{3.6}$ that is adopted for the diffuse ISM (Draine & Hensley 2021a). There are marked differences between the environments of the dust-producing circumstellar shells of the bright Wolf-Rayet stars and the diffuse ISM. Towards both sightlines, the stars have a factor ~ 3 higher reddening than what is typical for the diffuse ISM and indications of ice absorption at $6.1\ \mu\text{m}$ are found (Marchenko & Moffat 2017). Therefore, the silicate composition of the diffuse ISM is retained. Nevertheless, the analysis exemplifies that characterization of the silicate stoichiometry and particle shape by MIR spectro-polarization is viable. Unfortunately, such observations were recorded in the past century (Smith et al. 2000) and novel high-sensitive instrumentation is needed for detecting polarized MIR extinction in the diffuse ISM.

The polarized dust emission spectrum in the submm is observed by Planck Collaboration et al. (2014, 2020). If the polarized emission in the submm and the polarized extinction in the optical is due to the same grains then this ratio in principle includes information on the grain elongation (Krügel 2003). For the ratio of $850\ \mu\text{m}$ to V band polarization a characteristic value of

$$\tau_V \frac{P_{850\ \mu\text{m}}}{P_V} = 4.31 \quad (8)$$

is adopted by Hensley & Draine (2021). In the diffuse ISM variations for different sightlines are noted in the hydrogen column density N_H , $E(B - V)$, R_V , and hence τ_V (Eq.6).

3. Model

3.1. Dust populations

A dust model for the diffuse ISM is presented that shall be in line with present observational constraints: the $[\text{C}]/[\text{Si}]$ abundance ratio (Eq. 1), the spectral variation of the reddening, the starlight polarization, the diffuse galactic emission, and the polarized dust emission (Sec. 1). Two major grain materials are considered: amorphous silicates and carbon. Dust particles need to be of different sizes to fit the reddening and polarization curves. A power-law size distribution $dn(r)/dr \propto r^{-q}$ (Mathis et al. 1977) that ranges from the molecular domain ($r_- \sim 5\ \text{\AA}$) to a rather unconstrained upper size limit of several microns ($r_+ \lesssim 10\ \mu\text{m}$) is applied. Three different dust populations are distinguished:

1) *Nanoparticles* with sizes below 6 nm, which are in form of very small silicates (vSi), very small graphite (VSG), and PAHs. Two kinds of PAH are treated, small molecules having 30 C and 12 H atoms and clusters with 200 C and 40 H atoms, respectively. The cross-sections of the nanoparticles and PAHs are taken from Siebenmorgen et al. (2014).

2) *Large grains* with radii between 6 – 300 nm, which are partly aligned and of prolate shape with an axial ratio $a/b = 2$. Large grains are made of silicates (Si) and amorphous carbon (aC). Scattering, absorption, and polarization cross-sections of spheroids are computed with the procedure outlined in Sec. 3.3.

3) *Dark dust*, is included as a new additional grain component of micro-meter-sized particles. Dark dust grains are taken to be some kind of fluffy aggregates that are made up of porous composites of large silicate and large amorphous carbon grains that are sticking loosely together. The frosting of molecules on dark dust can be envisioned as an attractive reservoir of the reported O depletion but is not considered because of the missing detection of ice absorption bands in the diffuse ISM. Dark dust

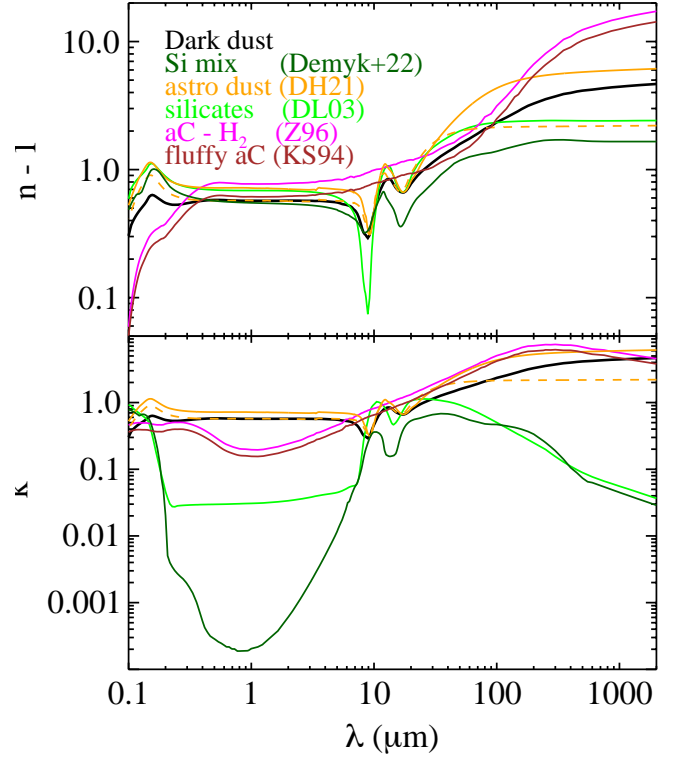


Fig. 5. Optical constants $n - 1$ (top) and k (bottom) for various grain materials.

particles are treated as spheres unless otherwise stated. For fluffy grains, there are only approximate methods for calculating the cross-sections. The numerical simple tool by Krügel & Siebenmorgen (1994) is used utilizing the Bruggemann mixing rule. An averaged complex dielectric function, $\epsilon = m^2$ is computed by solving

$$\sum_i f_i \frac{\epsilon_i - \epsilon_{av}}{\epsilon_i + 2\epsilon_{av}} = 0 \quad \text{with} \quad \sum_i f_i = 1, \quad (9)$$

where the volume fraction of each component i is denoted by f_i . The considered inclusions in a dark dust particle are: silicates with $f_{\text{Si}} = 0.5$, amorphous carbon $f_{\text{aC}} = 0.3$, and vacuum with $f_{\text{vac}} = 0.2$ to represent porosity, while ices are ignored.

3.2. Porosity

Optical constants $m = n - ik$ with $k \geq 0$ of various grain materials are displayed in Fig. 5. Optical constants are shown for the aC-H₂ mixture of amorphous carbon by Zubko et al. (1996), silicate and graphite by Draine (2003), and a 97:3 mix in mass of amorphous silicate grains with 2% vacuum inclusion that are composed of $\text{MgO}-0.5\ \text{SiO}_2$ and $\text{Mg}_{0.8}\text{Fe}_{0.2}^{2+}\text{SiO}_3$ using optical constants by Demyk et al. (2022) and as discussed in Sect. 6. The Si and aC grains differ by large in n and k , respectively.

By considering fluffy particles the optical constants are shifted to lower values and follow a similar spectral shape as for pure materials that do not have vacuum inclusions. This is seen in Fig. 5 by comparing aC-H₂ grains by Zubko et al. (1996) with fluffy aC (Krügel & Siebenmorgen 1994) with 20% vacuum inclusion and using Eq. (9). The spectral shape of the agglomerates by Draine & Hensley (2021a) is shown in Fig. 5 in orange

without (full line) and with 20% porosity (dashed), which can be compared with fluffy composites in black. The latter is a representation of dark dust. Again in the latter two sets similarities in the spectral shape of n and k are visible as well as a larger shift in the FIR/submm where differences in the slope become more pronounced. Also important is that by changing the vacuum content of materials the spectral slope remains unaltered. Thus the slope of the dust emissivity of a material, e.g. in the submm, does not change with porosity. For the same mass the strength of the dust emissivity increases by increasing the porosity because fluffy grains are larger than particles of the same material that have less or no vacuum inclusions.

3.3. Aligned spheroidal grains

The interstellar polarization phenomenon in the optical and IR/mm cannot be explained by spherical dust particles. Interstellar polarization of starlight and polarized dust emission is explained by partially aligned non-spherical dust grains that wobble and rotate about the axis of the greatest moment of inertia. Most simple representations of finite-sized non-spherical grains are spheroids. They are characterised by the ratio a/b between major and minor semi-axes. Spheroids can be either in form of oblates such as pancakes or prolates such as needles. The volume of a prolate is the same as a sphere with a radius given by $r^3 = a \cdot b^2$.

The dust optical depth at frequency ν is given by the product of the column density N_d of the dust along the sightline and the dust extinction cross-section $C_{\text{ext}} = C_{\text{abs}} + C_{\text{sca}}$, which is the sum of absorption and scattering

$$\tau(\nu) = N_d C_{\text{ext}}(\nu). \quad (10)$$

Linear polarization is

$$p(\nu) = N_d C_p(\nu), \quad (11)$$

where C_p is the linear polarization cross-section.

Physical processes that led to grain alignment are under debate and various mechanisms have been proposed, see reviewed by Voshchinnikov (2012) and Andersson et al. (2015). In picket fence (Dyck & Beichman 1974) a fraction of the grains is in perfect alignment while the other particles are randomly oriented. A modified version of it is used by Draine & Hensley (2021a), where it is assumed that the cross-sections along the **E** and **B** field depends on $\cos^2 \theta$ of the scattering angle (the angle between the wave vector **k** of the incoming light and the symmetry axis of the grain). There exist also non-magnetic alignment processes such as in gas streams of stellar winds or by an-isotropic illumination where photons are predominantly absorbed from one side of the particle. Radiative torque alignment has also become popular. In the Milky Way the direction of the dust-induced polarization in the optical is well correlated with the orientation of the magnetic field, which is derived from synchrotron emission in the radio. Hence magnetic fields are often taken to be responsible for the grain alignment in the ISM. In that picture, questions arise when estimating the relaxation times for the magnetic alignment of the grain in comparison to the time when the disorder is again established through collisions with gas atoms. For solving that puzzle supra-thermal grain rotation (at a frequency of 10^5 Hz) were proposed as well as (super-)paramagnetic or ferromagnetic relaxation. In the following the imperfect Davies-Greenstein mechanism (IDG) is applied in which Fe atoms in

the dust interact with the weak **B** field of the ISM. One advantage of IDG is that the orientation of a spinning and wobbling spheroid can be described mathematically in closed form. For angles ψ , φ , precision angle β , and magnetic field direction Ω , applied as in the notation by Hong & Greenberg (1980) and suffix TM for the transverse magnetic and TE for transverse electric polarization direction as in the notation by Bohren & Huffman (1983), the alignment function becomes

$$f(\beta) = \frac{\frac{r+0.1 \delta_0}{r+\delta_0} \sin \beta}{\left(\left(\frac{r+0.1 \delta_0}{r+\delta_0} \right)^2 \cos^2 \beta + \sin^2 \beta \right)^{3/2}}. \quad (12)$$

The alignment efficiency $\delta_0 \sim 0.1 - 10 \mu\text{m}$ (Das et al. 2010; Siebenmorgen et al. 2014) is related to the physical picture. It impacts the maximum of the polarization p_{max} but not the shape $p(\lambda)$ of the polarization (Voshchinnikov & Das 2008). The cross-sections are computed for given efficiency factors Q (Sec. 4.1) as average over the orientation of the wobbling particles

$$C_{\text{ext}}(\nu) = \frac{2}{\pi} \int (Q_{\text{ext}}^{\text{TM}} + Q_{\text{ext}}^{\text{TE}}) r^2 f(\beta) d\varphi d\Omega d\beta, \quad (13)$$

$$C_p(\nu) = \frac{1}{\pi} \int (Q_{\text{ext}}^{\text{TM}} - Q_{\text{ext}}^{\text{TE}}) r^2 f(\beta) \cos(2\psi) d\varphi d\Omega d\beta. \quad (14)$$

3.4. Reddening

The mass extinction cross-sections $K_{\text{ext},i}(r)$ ($\text{cm}^2/\text{g-dust}$) of a dust particle of population $i \in \{\text{Si, aC, vSi, VSG, Dark}\}$, radius r , and density ρ_i is

$$K_{\text{ext},i}(r) = \frac{m_i}{\frac{4\pi}{3} \rho_i} \frac{r^{-q}}{\int_{r_{-i}}^{r_{+i}} r^{3-q} dr} C_{\text{ext},i}(r). \quad (15)$$

The cross-sections C are derived using efficiency factors Q , which are computed for spheres by Mie theory and spheroids as in Sec. 3.3. The relative weight, also called specific mass, in 1 g of dust in component i , is

$$m_i = \frac{\frac{[X]}{[H]}_i \mu_X}{\left(\frac{[C]}{[H]}_{\text{aC}} + \frac{[C]}{[H]}_{\text{gr}} + \frac{[C]}{[H]}_{\text{PAH}} \right) \mu_C + \left(\frac{[\text{Si}]}{[H]}_{\text{Si}} + \frac{[\text{Si}]}{[H]}_{\text{sSi}} \right) \mu_{\text{Si}}}, \quad (16)$$

where relative dust abundances of element X, which is either C or Si, with respect to H are denoted by $[X]/[H]_i$ together with a subscript i for each of the dust population, $\mu_C = 12$ is the molecular weight of carbon, $\mu_{\text{Si}} = 134.46$ that of silicate grains with bulk densities $\rho_C \sim 1.6 \text{ g/cm}^3$ and $\rho_{\text{Si}} \sim 3.41 \text{ g/cm}^3$ (Draine & Hensley 2021a), respectively. The specific mass for PAH is computed in similar terms (Siebenmorgen et al. 2014). Specifying the mass extinction cross-section per gram of dust has the advantage that only relative element abundances $[X]/[H]_i$ need to be specified instead of the more uncertain absolute solid-phase element abundances (in ppm), which however, may be used as a guideline. The total mass extinction cross-section averaged over the dust size distribution in $\text{cm}^2/\text{g-dust}$ is

$$K_{\text{ext}} = \sum_i \int_{r_{-}}^{r_{+}} K_{\text{ext},i}(r) dr. \quad (17)$$

The wavelength dependence in the above expressions (Eq. 13 - 17) is dropped for clarity. The reddening curve of the dust model is derived using Eqs. (5, 6) and noting K as the mass extinction cross-section

$$E(\lambda) = \frac{K_V}{K_B - K_V} \left(\frac{K(\lambda)}{K_V} - 1 \right). \quad (18)$$

Note by using R_V (Eq. 5) that the reddening $E(\lambda)$ is derived self-consistently from the dust model without extrapolation to infinite wavelengths.

3.5. Emission

The emission $\epsilon_{\nu,i}(r)$ of a dust particle of radius r , grain material i at frequency ν is

$$\epsilon_{\nu,i}(r) = K_{\nu,i}^{abs}(r) \int P_i(r, T) B_\nu(T) dT, \quad (19)$$

where $K_{\nu,i}^{abs}$ is the mass absorption cross-section (Eq. 15), $B_\nu(T)$ is the Planck function, and $P_i(r, T)$ is the temperature distribution function that gives the probability of finding a particle of material i and radius r at temperature T . This function is determined from the energy balance between the emission and absorption of photons from the mean intensity J_ν , for which here the ISRF by Mathis et al. (1983) is applied

$$\int K_{\nu,i}^{abs}(r) J_\nu(T) d\nu = \int K_{\nu,i}^{abs}(r) P_i(r, T) B_\nu(T) dT d\nu. \quad (20)$$

It is evaluated using an iterative scheme that is described by Krügel (2008). The $P(T)$ function only needs to be evaluated for small grains as it approaches a δ -function for large particles where the temperature fluctuates very little around the equilibrium temperature. The total emission ϵ_ν of the dust at frequency ν is given as the sum of the emission $\epsilon_{\nu,i}(r)$ of all dust components.

3.6. Gas-to-dust mass ratio

Observations of the diffuse emission of the galaxy are given per hydrogen column density, $\lambda I_\lambda/N_H$ (erg/s/sr/H-atom), whereas the dust emission of the model is computed (Eq. (19) per dust mass (erg/s/sr/g-dust). For the necessary conversion of the dust to the gas column densities often a procedure is applied assuming that for sightlines in the diffuse ISM the extinction is proportional to the hydrogen column density $A_V = 1.086 \times \tau_V \propto N_H$. In addition, one presumes that A_V can be reasonably estimated by applying a mean value of the total-to-selective extinction and the derived reddening using $A_V = R_V \times E(B - V)$. Further, one assumes that the ratio $\zeta = N_H/E(B - V)$ stays roughly constant in the ISM. Traditionally $\zeta = 5.8$ (10^{21} H cm $^{-2}$ mag $^{-1}$) is applied, which is derived from 75 sightlines observed within 3.4 kpc by Copernicus (Bohlin et al. 1978). For translucent clouds at $\tau_V \gtrsim 0.5$ observed by FUSE $\zeta = 5.94 \pm 0.37$, from here onwards in units as before (Rachford et al. 2009), and from X-ray observations $\zeta \sim 6.3 - 6.5$ (Zhu et al. 2017) using $R_V = 3.1$. However, striking differences are derived from radio observations of HI with lower values in earlier work of $\zeta = 4.6$ (Mirabel & Gergely 1979) and 5.1 (Knapp & Kerr 1974) or higher values in recent studies of $\zeta = 8.3$ (Liszt 2014), 8.8 (Lenz et al. 2017)

and 9.4 (Nguyen et al. 2018). Dust emission of the diffuse ISM is observed towards high galactic latitudes where there is less dust per H atom as in the Galactic plane so that the latter value of ζ has been favoured by Hensley & Draine (2021).

In the procedure applied here these uncertainties in ζ , R_V , and $E(B - V)$ are avoided. A gas-to-dust mass ratio $M_{\text{gas}}/M_{\text{dust}}$ is introduced that is given by scaling the dust emission spectrum of Eq. (19) to the Planck data at 350 μm . The observed emission is fit by

$$\frac{\lambda I_\lambda}{N_H} = \frac{M_{\text{dust}}}{M_{\text{gas}}} \frac{\lambda \epsilon_\lambda}{m_p}, \quad (21)$$

with H-atom mass m_p . The procedure has the advantage that $M_{\text{gas}}/M_{\text{dust}}$ is derived in the same direction as to where the data were taken. Of course, uncertainties that arise due to possible variations in the strength of the ISRF towards the observed fields remain and are assumed to be small.

3.7. Polarized extinction

Starlight polarization is derived by dichroic extinction of the dust (Eqs. 10 - 11, 14)

$$p(\nu)/\tau_V = K_p(\nu)/K_{\text{ext},V}, \quad (22)$$

K_p denotes the total linear mass polarization cross-section (cm 2 /g-dust) and is computed similar to K_{ext} by replacing in Eq. (15) the cross-section $C_{\text{ext},i}$ (Eq. 13) with $C_{p,i}$ (Eq. 14).

3.8. Polarized emission

Polarized dust emission of component i is computed by integrating over the minimum $r_{\text{pol},i}^-$ to maximum $r_{\text{pol},i}^+$ alignment radii

$$\epsilon_{\text{pol},i}(\nu) = \int_{r_{\text{pol},i}^-}^{r_{\text{pol},i}^+} K_{\text{pol},i}(\nu, r) B_\nu(T) dr. \quad (23)$$

Note that $C_p = K_p = 0$ for spherical or non-aligned grains. The total polarized dust emission ϵ_{pol} is given as the sum of the polarized emission $\epsilon_{\text{pol},i}$ of all components contributing to the polarization. These are large aC and Si prolate grains and dark dust when also considered of prolate shape. Polarization by nanoparticles is not considered.

4. Method

The dust model is confronted with the observational constraints presented in Sec. 2. As described by Zubko et al. (2004) the fitting procedure leads to a typical ill-posed inversion problem where the solution is extremely sensitive to small changes in input data and with several priors such as the size distribution or grain composition as unknowns. Therefore, a least χ^2 -technique is applied for which first, a method for finding the best fit of the reddening curve is presented that respects dust abundance constraints (Eq. 1). For that model, the parameters which impact the shape of the starlight polarization are varied to find the best fit to the mean Serkowski curve. The latter model is then compared to the diffuse galactic emission, which requires applying a gas-to-dust mass ratio. The flatness in the submm/mm polarization spectrum as well as the ratio of the starlight polarization to

submm polarization is tested. The parameter space of the model is explored and the goodness of the fit is quantified as the sum of differences between observations and the model, each squared and divided by the observed data. For the reddening curve the goodness parameter is denoted by χ_r^2 and for the polarized extinction χ_p^2 , respectively.

4.1. Cross-sections

The various dust cross-sections for extinction, scattering, and polarization are computed in the spectral range between $90 \text{ nm} \lesssim \lambda \lesssim 1 \text{ cm}$ and for grain radii range between $5 \text{ \AA} \lesssim r \lesssim 10 \text{ }\mu\text{m}$. The challenge is computing the efficiency factors $Q = C/\pi r^2$ for the two polarization directions of elongated particles (Eqs. 13, 14). For small size parameter $x = 2\pi r/\lambda \ll 1$ the Rayleigh approximation might be used (Krügel 2008). For typical ISM grains with sizes $r \leq 0.3 \text{ }\mu\text{m}$ scattering becomes small at $\lambda \gtrsim 8 \text{ }\mu\text{m}$ and the Rayleigh limit $2\pi r \ll \lambda$ is held. The Rayleigh approximation breaks at $x \gtrsim 0.25$ (Voshchinnikov 2004; Draine & Hensley 2021b) and cannot be used in most of the interesting cases. Electromagnetic absorption and scattering by spheroids can be treated using different methods. A numerical solution of separation of variables in the Maxwell equation is presented by Voshchinnikov & Farafonov (1993). The discrete dipole approximation by Draine & Flatau (1994) offers a possibility for the treatment of various grain structures. In addition, the extended boundary condition method by Mishchenko (2000) also known as T-matrix approximation is available. The methods have been tested extensively by the authors and excellent agreement at $x \sim 10$ is exemplified (Draine & Hensley 2021b). The program³ by Voshchinnikov & Farafonov (1993) is used. It returns for a given complex optical constant m and the size parameter x , the efficiency factors $Q_{\text{ext}}^{\text{TM}}(x, m)$ and $Q_{\text{ext}}^{\text{TE}}(x, m)$ (Eqs. 13 - 14). The code converges up to $|m - 1| x \lesssim 25$, which is found to be at larger x than in most of the other applications.

4.2. Fitting procedure

The radial grid in grain size is ascending using $r_{i+1} = 1.05 r_i$. Intermediate radii between two consecutive grid points are linearly interpolated when necessary. The upper radius of the dark dust is varied for six values of $r_{\text{Dark}}^+ = 0, 0.5, 0.8, 1.0, 5.0$, and $10 \text{ }\mu\text{m}$, where $r_{\text{Dark}}^+ = 0 \text{ }\mu\text{m}$ refers to a model without dark dust. Models assuming even larger grains were also inspected without finding striking features. By assuming a continuous distribution in the particle size the minimum radius of the dark dust follows that of the maximum radius of the large aC and Si grains, hence $r_{\text{Dark}}^- = \max(r_{\text{ac}}^+, r_{\text{Si}}^+)$. Models fitting the observational constraints show $r_{\text{ac}}^+ < r_{\text{Si}}^+$. The exponent of the size distribution q is kept as a free parameter, however, the same q is used for all three dust populations. After some experiments the mass in dark dust is adopted to be 10 % of the total dust mass; this parameter will be fine-tuned when fitting the dust emission in the mm range. Dust abundances are given in the model in relative terms and one parameter can be kept fixed, and $[\text{Si}]/[\text{H}]_{\text{Si}} = 15 \text{ ppm}$ is set.

The polarization data are solely fit by large grains unless otherwise specified. A detailed fit to the Serkowski curve is obtained when the alignment of both large grain materials aC and Si differ. Models fitting the absolute values of the polarization shall be applied towards individual sightlines that are dominated by a single absorbing cloud (Siebenmorgen et al. 2018b). Hence parameters that change p_{max} but do not affect the spectral shape of the polar-

ization are held constant (Voshchinnikov 2012). This concerns the magnetic field direction that is set to $\Omega = 60^\circ$, the ratio of the major axis of prolates $a/b = 2$, and the alignment efficiency of aC grains $\delta_0(\text{aC}) = 10 \text{ }\mu\text{m}$, while variations of Si grains of $\delta_0(\text{Si}) = 0.5, 1.0$, and $10 \text{ }\mu\text{m}$ are explored. The maximum alignment radius r_{pol}^+ shows no strong variations of the starlight polarization spectrum whereas the minimum alignment radius r_{pol}^+ has a strong impact (Siebenmorgen et al. 2014). As maximum alignment radius the upper radius derived from the reddening fit is applied, $r_{\text{pol, Si}}^+ = r_{\text{Si}}^+$ and $r_{\text{pol, aC}}^+ = r_{\text{ac}}^+$, respectively. The minimum alignment radius is taken as a free parameter for aC and Si grains. The Si grains are dominating the polarization curve at shorter wavelengths and generally $r_{\text{pol, Si}}^- \lesssim r_{\text{pol, aC}}^-$ is hold.

The reddening curve is fit using the 3×6 values as above for δ_0 and r_{Dark}^+ , which have minor impact on $E_{\text{mod}}(\lambda)$ and in addition the seven parameters of the dust model: $[\text{C}]/[\text{H}]_{\text{aC}}$, $[\text{C}]/[\text{H}]_{\text{VSG}}$, $[\text{C}]/[\text{H}]_{\text{PAH}}$, $[\text{Si}]/[\text{H}]_{\text{vSi}}$, q , r_{ac}^+ , and r_{Si}^+ . A set of best fit parameters are computed by a least χ^2 -technique utilizing the Levenberg–Marquardt algorithm as implemented in MPFIT⁴ (Markwardt 2009). The algorithm can find local minima. The challenge is to identify the global $\chi_r^2(r)$ minimum of the reddening curve fit. This minimum is derived by starting the algorithm using many different initial parameter values. As an initial guess the mean dust parameters of ISM sightlines fit by Siebenmorgen et al. (2018b) are applied: $[\text{C}]/[\text{H}]_{\text{aC}} = 67$, $[\text{Si}]/[\text{H}]_{\text{vSi}} = 5$, $[\text{C}]/[\text{H}]_{\text{VSG}} = 17$, $[\text{C}]/[\text{H}]_{\text{PAH}} = 10$ (ppm), and $q = 3$. In addition one initial radius r_i is selected out of 12 different upper sizes of large aC and Si grains of the radial grid between $180 \lesssim r_i = r_{\text{ac}}^+ = r_{\text{Si}}^+ \lesssim 300 \text{ (nm)}$. This limit is based on an exploration of the model space which has shown that start values of $r_i > 300 \text{ nm}$ did not result in acceptable solutions. An initial MPFIT run is started keeping $r_{\text{ac}}^+ = r_{\text{Si}}^+$ fixed and after converging the resulting 5 parameters $[\text{C}]/[\text{H}]_{\text{aC}}$, $[\text{C}]/[\text{H}]_{\text{VSG}}$, $[\text{C}]/[\text{H}]_{\text{PAH}}$, $[\text{C}]/[\text{H}]_{\text{vSi}}$, and q are held constant, while MPFIT is re-started a second time with r_{ac}^+ and r_{Si}^+ set as free.

This procedure is iterated, generally twice, until χ_r^2 is not reduced further. Then the starlight polarization curve is fit minimizing $\chi_p^2(\delta_0(\text{Si}), r_{\text{pol}}^-(\text{Si}), r_{\text{pol}}^-(\text{aC}))$ between the observed Serkowski curve (Eq. 7) and the dust model (Eq. 22). In that method the 7 best-fit dust parameters derived from the reddening curve procedure are held constant and χ_p^2 is computed for the three $\delta_0(\text{Si})$ and all combinations of the minimum alignment radii of aC and Si grains between $6 \text{ nm} < r_{\text{pol}}^- < \min(r_{\text{ac}}^+, r_{\text{Si}}^+)$, respectively.

For keeping the computational time within reasonable limits the fitting procedure is vectorized by running calls to MPFIT with the many different start values parallel.

5. Results

A $r_{\text{Dark}}^+ \times \delta_0(\text{Si}) \times r_{\text{ac}}^+$ tuple with $3 \times 6 \times 12$ models is computed applying the procedure of Sec. 4.2. The model grid includes for each combination of $\delta_0(\text{Si})$ and r_{Dark}^+ , the seven derived best-fit parameters to the reddening $[\text{C}]/[\text{H}]_{\text{aC}}$, $[\text{C}]/[\text{H}]_{\text{VSG}}$, $[\text{C}]/[\text{H}]_{\text{PAH}}$, $[\text{C}]/[\text{H}]_{\text{vSi}}$, q , r_{ac}^+ , r_{Si}^+ , the two best fit parameters to the starlight polarization r_{ac}^+ , r_{Si}^+ , and the corresponding goodness parameters χ_r^2 and χ_p^2 , respectively. The majority of models provide a reasonable fit to the reddening and polarization curves but do not respect the abundance constraint of $[\text{C}]/[\text{Si}] \lesssim 5.25$ (Eq. 1) and are rejected. Out of the 216 models, 27 are consistent with the

³ Fortran code SPVV8.5 kindly provided by N. Voshchinnikov[†].

⁴ <http://purl.com/net/mpfit>

Table 1. Parameters of the dark dust model for the diffuse ISM using Draine (2003) optical constants for amorphous silicate grains.

1	2	3	4	5	6	7	8	9	10	11	12	13	14	15	16	17	18
Model		Mass ratio (%) Abundances (ppm)						Sizes						Derived quantities			
r_{Dark}^+ (μm)	χ^2 N ($\chi^2 < 1$)	m_{Dark}	m_{Si} [Si]/[H] _{Si}	m_{vSi} [Si]/[H] _{vSi}	m_{aC} [C]/[H] _{aC}	m_{VSG} [C]/[H] _{VSG}	m_{PAH} [C]/[H] _{PAH}	q	r_{Si}^+ (nm)	r_{aC}^+ (nm)	$r_{\text{pol, Si}}^-$ (nm)	$r_{\text{pol, aC}}^-$ (nm)	$\delta_0(\text{Si})$ (μm)	[C]/[Si]	$M_{\text{gas}}/M_{\text{dust}}$	R_V	τ_V
0 [‡]	0.5 0	-	46 15	23 7	25 92	4 15	3 10	3.0	243	203	80	166	0.5	5.2	125	3.09	1.01
0.75 [‡]	0.7 0	7	43 15	20 7	24 96	4 15	2 8	3.0	228	201	84	166	0.5	5.5	138	3.16	1.42
1	0.6 5	6	44 15	21 7	23 88	4 15	2 8	3.0	217	207	76	143	1.0	5.0	131	3.09	1.37
5	0.6 3	7	41 15	22 8	23 95	3 13	3 11	2.9	220	208	80	166	0.5	5.2	124	3.11	1.30
10	0.7 3	6	49 15	17 6	22 91	3 14	2 8	3.1	239	222	88	183	0.5	4.6	124	3.18	1.36

Notes: In Col. (1) the upper radius of the dark dust agglomerates r_{Dark}^+ is specified, in Col. (2) the goodness χ^2 of the best fit model and below the number N of models that are consistent with the observational constraints and fit the reddening and Serkowski curve at $\chi^2 < 1$. Corresponding parameters of the specific mass in % per gram dust (Col. 3-8) of dark dust as lower limit m_{Dark} , and for large silicates m_{Si} , nano-sized silicates m_{vSi} , large amorphous carbon m_{aC} , very small graphite m_{VSG} , and PAHs m_{PAH} . Below, in the second row of Col. 3-8, exemplified dust abundances [X]/[H] (ppm) are given by adopting [Si]/[H] = 15 ppm in large silicates. Col. (9) gives the exponent of the dust size distribution q . The upper radius of large silicates r_{Si}^+ (Col. 10) and amorphous carbon r_{aC}^+ (Col. 11), their lower alignment radii $r_{\text{pol, Si}}^-$ and $r_{\text{pol, aC}}^-$ (Col. 12, 13), respectively, and the alignment efficiency (Col. 14) of large silicates $\delta_0(\text{Si})$ is given. Derived quantities of the dust models are given for the dust abundance ratio [C]/[Si] (Col. 15), the gas-to-dust mass ratio $M_{\text{gas}}/M_{\text{dust}}$ (Col. 16), the total-to-selective extinction R_V (Eq. 5, Col. 17), and the optical depth (Col. 18) that matches the optical-to-submm polarization ratio of $p_{850\mu\text{m}}/(p_V/\tau_V) = 4.31$ (Eq. 8) by Planck Collaboration et al. (2020).

[‡] Model violates abundance constrain (Eq. 1).

[‡] Models without dark dust do not fit the Planck Collaboration et al. (2015, 2020) data at ≥ 0.8 mm.

dust abundance ratio (Eq. 1) and 22 remain after applying a 3σ outlier rejection in χ_r^2 and χ_p^2 , respectively. Their χ_r^2 and χ_p^2 are each normalised to a mean of one so that they can be combined. The model that simultaneously fits both curves best is selected from a minimum χ^2 condition where each parameter is given the same weight using

$$\chi^2(r_{\text{Dark}}^+) = \frac{7}{10} \chi_r^2 + \frac{3}{10} \chi_p^2. \quad (24)$$

Model parameters with the minimum in $\chi^2 < 1$ for given r_{Dark}^+ are listed in Table 1. These models agree with the observed reddening and polarization. Models that ignore dark dust ($r_{\text{Dark}}^+ = 0\mu\text{m}$) underpredict the observed emission in the Planck bands at wavelength ≥ 0.8 mm (Fig. 6). There is no model with $r_{\text{Dark}}^+ = 0.5\mu\text{m}$ that fits reddening and polarization at $\chi^2 \lesssim 1$.

For $r_{\text{Dark}}^+ = 0.75\mu\text{m}$ there is only one such model, it has $\chi^2 = 0.7$ but [C]/[Si] = 5.5 (Table 1, Col. 15). Hence it violates the abundance constraint (Eq. 1). Therefore, at $r_{\text{Dark}}^+ < 1\mu\text{m}$ no model is consistent with the observations at $\chi^2 < 1$ and the number of such models is $N(\chi^2 < 1) = 0$ (Table 1, Col. 2).

Models that agree with the observing constraints consider micrometre-sized dark dust particles at $r_{\text{Dark}}^+ \geq 1\mu\text{m}$. The global minimum over all models is found for $r_{\text{Dark}}^+ = 1\mu\text{m}$ at $\chi^2 = 0.6$. For this radius, there are 5 models at $\chi^2 < 1$. The best fitting models of $r_{\text{Dark}}^+ = 5$ and $10\mu\text{m}$ have similar χ^2 ($\lesssim 0.7$), respectively. Their fits to the observed reddening, polarization, and dust emission are of similar quality as for the best fit $r_{\text{Dark}}^+ = 1\mu\text{m}$ model. For each of these radii there are $N(\chi^2 < 1) = 3$ models that fit the reddening and polarization at $\chi^2 < 1$ and fulfill the abundance constraint [C]/[Si] < 5.25 (Eq. 1). The scatter in the individual parameters between the selected models is small (Table 1). The peak-to-peak variations in the abundances for a given dust population (Table 1, Col. 3-8) and the particular size parameters stay well below 10 % (Table 1, Col. 10-13).

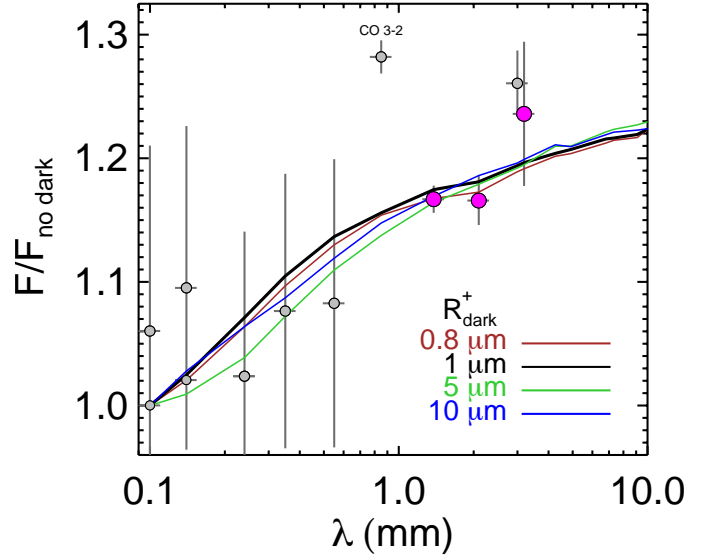


Fig. 6. Ratio $F/F_{\text{no dark}}$ of the dark dust models and the observed fluxes (circles, using data as in Fig. 2) divided by the model neglecting dark dust ($r_{\text{Dark}}^+ = 0\mu\text{m}$). Best fits (lines) to the 1.4 mm and 2.1 mm data derived by varying the amount of dark dust m_{Dark} for models with $r_{\text{Dark}}^+ \geq 0.75\mu\text{m}$ as labelled. Parameters as in Table 1.

The fit of the $r_{\text{Dark}}^+ = 1\mu\text{m}$ model with parameters of Table 1 to the observed reddening and extinction is shown in Fig. 1. The individual dust components show the known behaviour of the reddening: nanoparticles are responsible for the rise in the far UV, PAH and VSG fit the 2175Å extinction bump, and large aC and Si grains give a rather flat contribution from the U band to shorter wavelengths. Remarkable is the constant reddening of dark dust from the far UV to the NIR, up to wavelengths, which are similar to the upper grain radius r_{Dark}^+ , which is for that model

at $\sim 1 \mu\text{m}$ (Fig. 1, right). The non-dispersed reddening provided by dark dust to the UBVRI bands is significant. Dark dust causes extra dimming of light not accounted for in dust models omitting this component.

The model fit to the observed starlight polarization curve is shown in Fig. 3. For deriving such a detailed fit it is necessary that both large Si and aC grains contribute to the polarization and that both dust materials have distinct characteristics in the alignment radii and the polarization efficiency (cmp. Col 10-14 of Table 1). Polarized extinction is dominated in the UV by Si grains and in the R band by aC grains.

Dark dust treated as prolates with axial ratio $a/b = 2$, $\delta_o = 10 \mu\text{m}$, and $r_{\text{Dark}}^+ = 1 \mu\text{m}$ contribute to p/p_{max} most near $\sim 2 \mu\text{m}$ at less than a few percent.

Dark dust polarized extinction in the MIR is shown for models with $r_{\text{Dark}}^+ = 1 \mu\text{m}$ and $r_{\text{Dark}}^+ = 10 \mu\text{m}$ in Fig. 4, respectively. Large aC grains show a flat polarization at $\sim 20\%$ of the maximum MIR polarization p_{max} , while Si grains dominate the spectrum. Dark dust, even when elongated and aligned particles are assumed, contributes to the normalised MIR polarization by less than $p/p_{\text{max}} < 10\%$. The composite polarization spectrum derived from observations of two Wolf-Rayet stars refers to greatly distinct environments from the diffuse ISM. Nevertheless, the data are shown in Fig. 4 demonstrates the capabilities of using MIR polarization as a method to estimate the stoichiometry of silicate grains.

The dust emission of the models is compared to the diffuse emission of the ISM that is observed at high galactic latitudes normalised per H atom and is shown for the best fit $r_{\text{Dark}}^+ = 1 \mu\text{m}$ model in Fig. 2. The models are scaled to the 0.3 mm data, which allows for an estimate of the gas-to-mass ratio (Eq. 21). A mean of $M_{\text{gas}}/M_{\text{dust}} = 126 \pm 4$ is derived for the best fitting models (Table 1, Col 16). The emission of the individual dust components shows the known behaviour: nanoparticles are responsible for the MIR emission, PAH to the IR emission bands and large grains dominate the FIR/submm. The lowest temperature of aC grains is 16.8 K, that of Si grains 14.8 K, and dark dust is as cold as 12.3 K for the $r_{\text{Dark}}^+ = 1 \mu\text{m}$ model and 8.1 K for the $r_{\text{Dark}}^+ = 10 \mu\text{m}$, respectively. Dark dust emission peaks at $\sim 0.2 \text{ mm}$ and becomes a more important contributor in the mm range where it even overshines the emission by large Si grains. This is as expected by comparing the extinction cross-sections of the different dust ingredients. Noticeable in Fig. 7 are the various PAH features, the $9.7 \mu\text{m}$ and $18 \mu\text{m}$ bands of the silicates, and that aC grains dominate the cross-sections over the entire spectrum at $\lambda \gtrsim 0.1 \mu\text{m}$, except near the $9.7 \mu\text{m}$ band. Furthermore, in the submm, the cross-section of dark dust has similar strength as that of Si grains. Dark dust shows in the mm range a slightly shallower decline in the emissivity than the other grains, which is as expected inspecting the imaginary part k of the optical constants (Sec. 3.2).

Models that exclude dark dust or models that do not alter the FIR/mm spectral index of the grain emissivity do not account for the dust emission observed by Planck Collaboration et al. (2015, 2020). This is exemplified in Fig. 6. The observed flux F is divided by the flux $F_{\text{no dark}}$ of the models that do not consider dark dust ($r_{\text{Dark}}^+ = 0 \mu\text{m}$, Table 1). The latter is a kind of Siebenmorgen et al. (2014) model; they include non-porous prolate grains and fit the DIRBE and Planck data up to 0.35 mm. These models are at $F/F_{\text{no dark}} \sim 1$ in Fig. 6. They systematically underpredict the emission in the Planck bands at 0.8 – 3 mm by 15 – 30%, which is significant considering the unprecedented precision of the Planck data. Fluffy and spheroidal grains show greater dust emissivity in the FIR/mm range than do non-porous and spher-

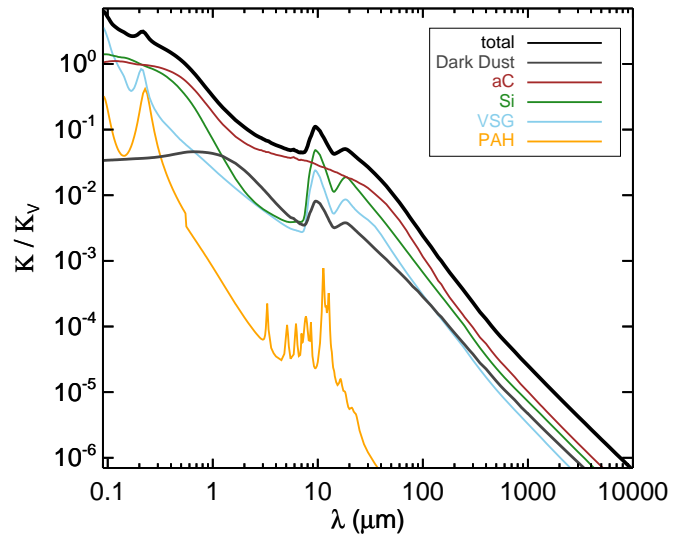


Fig. 7. Total extinction cross-section normalized to V for the $r_{\text{Dark}}^+ = 1 \mu\text{m}$ model (Table 1) with individual components as labelled.

ical grains of the same mass. The FIR/mm spectral slope of the dust emissivity stays invariable by increasing the porosity or the axial ratio of the spheroidal particles (cmp. Fig. 5 and Fig. 3 in Siebenmorgen et al. (2014)). Hence for fitting the emission in the mm range one must either change the spectral index of the dust emissivity by a suitable set of optical constants (Draine & Hensley 2021a) or include dark dust.

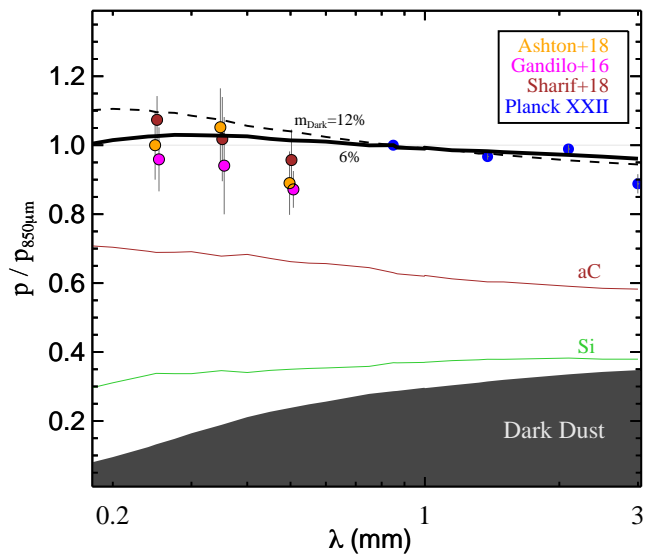


Fig. 8. Polarized emission of the diffuse ISM between 0.2 – 3 mm normalized to the polarization at $850 \mu\text{m}$. Observations (circles) with 1σ error bars in blue by Planck Collaboration et al. (2015, 2020), in magenta by Gandilo et al. (2016), in brown by Shariff et al. (2019), in orange by Ashton et al. (2018); as tabulated by Hensley & Draine (2021). Model with $r_{\text{Dark}}^+ = 1 \mu\text{m}$ (Table 1) and $m_{\text{Dark}} = 6\%$ of mass in dark dust (full line), the contributions (dashed) from large amorphous carbon (brown) and large silicate grains (green) as well as the total polarization fraction adopting $m_{\text{Dark}} = 12\%$ (dashed) is shown. The contribution from dark dust when treated as prolate particles are indicated by the area in grey.

The Planck bandpasses at 0.85 mm and 3 mm includes dust and other emission components such as the CO (3 – 2) or CO (1 – 2) line transitions, and at longer wavelengths free-free

or synchrotron radiation (Galamez et al. 2014). The two least contaminated bandpasses near 1.4 mm and 2.1 mm are used to estimate a lower limit of the amount of dark dust. The mass of dark dust is varied in the $r_{\text{Dark}}^+ \gtrsim 0.75 \mu\text{m}$ models until a best fit is found. Typically the mass in dark dust is at least $m_{\text{Dark}} \gtrsim 6\%$ of the total dust mass (Table 1, Col. 3) to fit the Planck observed emission.

The polarized dust emission at $\lambda \gtrsim 0.85 \mu\text{m}$ is observed by Planck Collaboration et al. (2015, 2020) and between $0.25 \gtrsim \lambda \gtrsim 0.85 \mu\text{m}$ for selected areas on the sky by BLASTPol (Gandilo et al. 2016; Ashton et al. 2018; Shariff et al. 2019). The polarization spectrum normalised to the fractional polarization at 0.85 mm is tabulated by Hensley & Draine (2021) and is shown in Fig. 8. It features an astonishingly flat spectrum that is within 1σ of 11% constant and challenges several dust models (Draine & Hensley 2021a). The best fit of the $r_{\text{Dark}}^+ = 1 \mu\text{m}$ dark dust model to the polarized emission spectrum is shown in Fig. 8 using parameters of Table 1. The total fractional FIR/mm polarization spectrum of the model is within $\sim 5\%$ constant and aC grains are the dominating contributor over the Si grains.

Dark dust when treated as prolate particles and alignment efficiency as aC grains give in the FIR a contribution of $\lesssim 10\%$ and in the mm range $\sim 35\%$ to the total polarization. The flatness of the submm/mm polarization spectrum provides an upper limit of the total amount of dark dust. This is shown in Fig. 2 where the polarization in the FIR is overestimated when increasing the dark dust mass to $m_{\text{Dark}} \gtrsim 12\%$ of the total dust mass.

The consistency of the models between optical and submm polarization is verified. Polarized extinction and polarized emission are tightly connected when produced by the same grains. For the diffuse ISM, a characteristic value is provided by Planck Collaboration et al. (2020) and is given in Eq. 8. The dark dust models cope with this optical-to-submm polarization ratio by adopting an optical depth of $1.3 \lesssim \tau_V \lesssim 1.37$ (Col. 18, Table 1). This is somewhat smaller than derived for sightlines with translucent clouds by Guillet et al. (2018), which have a slightly larger reddening than the diffuse ISM. The optical depth is converted to a dust reddening using the model-derived total-to-selective extinction R_V (Eq. 5). The reddening of the models is $E(B - V) = \tau_V/1.086/R_V$ (Col. 17-18 of Table 1) and range between 0.40 – 0.42 mag, which is in good agreement with the observationally derived mean of 0.45 mag (Fitzpatrick & Massa 2007).

6. Laboratory studies of cosmic dust analogous

Laboratory studies of cosmic dust analogous foster our knowledge in several research fields (Jäger et al. 2020): The experiments enlighten our understanding of processes leading to the formation or destruction of dust particles (Jones et al. 1994), the growth of grains to pebbles and planetesimals, and how dust eventually evolves into planets (Wurm & Blum 1998; Blum & Wurm 2008; Wurm & Teiser 2021). In the laboratory, chemical reaction paths of interstellar gas with charged or uncharged dust and nanoparticles and their interaction on the grain surfaces can be simulated (Salama et al. 1996; Herbst 2001; Jones 2021). Scattering matrices and phase functions of several irregular shaped particles have been measured (Muñoz et al. 2020).

Experimental results of optical constants for a range of dust materials have been obtained. Although, they are limited in the wavelength coverage (Dorschner et al. (1995); Mennella et al. (1998); Jäger et al. (2003), see the Heidelberg - Jena - St. Pe-

tersburg database ⁵). Models aiming to explain simultaneously the dust absorption and emission of polarized and unpolarised light require a consistent set of optical constants from the Lyman limit to about 1 cm, at least. In that wavelength range, optical constants derived from laboratory experiments are available for various carbon materials. These have been incorporated in dust models; see Zubko et al. (2004) for a comprehensive study. For amorphous silicate grains, a complete set of laboratory-derived optical constants suited for dust modelling was not available until the work by Demyk et al. (2022). Commonly, and as used in Sect. 4.2, the semi-empirical set by Draine (2003) is applied. These optical constants are based on laboratory measurements in the UV/optical by Huffman & Stapp (1973), on observations in the NIR and MIR, and some extrapolation by a power-law to longer wavelengths (Draine & Lee 1984). The same extrapolation is used by Jones et al. (2017), who considered in the UV/optical range optical constants of amorphous silicate dust by Scott & Duley (1996) and added metallic Fe and FeS inclusions to reproduce NIR observations. The exponent of the power-law was modified by Draine & Hensley (2021a) to accommodate the deficit submm/mm emission that was present in all of the previous dust models when confronted with the observations by the Planck mission (Ysard 2020).

Recently, Demyk et al. (2022) calculated optical constants between $10^{-2} - 10^5 \mu\text{m}$ of four Mg-rich glassy silicate dust particles with stoichiometry from about enstatite to olivine and eight samples of Mg- and Fe-rich silicates with stoichiometry close to pyroxene. For the samples, the mass absorption coefficients were measured at temperatures between 10 – 300 K and between 5 to $\sim 1000 \mu\text{m}$ (Demyk et al. 2017a,b). The optical constants of the samples show at temperatures above 30 K and wavelengths $\gtrsim 80 \mu\text{m}$ a significant temperature dependence. The dust absorption cross section at 300 K is increased by about one order of magnitude when compared to the sample measured at 30 K. This temperature dependence of the cross-section has so far been neglected in dust models. It results in an overestimate of the derived dust masses that is important for environments where dust is heated to such high temperatures (Fanciullo et al. 2020). The optical constants remain constant between 10 K and 30 K. In the diffuse ISM of the Milky Way the temperatures of large grains stay below ~ 20 K. Demyk et al. (2022) adopted in the wavelength range between 0.5 to $1 \mu\text{m}$, the refractive indices as measured for similar kinds of amorphous silicate grains by Dorschner et al. (1995) and Jäger et al. (2003). The extrapolation of the measurements to the entire wavelength range is a delicate issue. Besides the numerical challenges, detailed knowledge of the sample is required such as the bulk density of the materials, the grain shapes and structures, as well as the particle size distribution of the agglomerates. These parameters were derived by investigating images of the samples obtained by using Transmission Electron Microscopy (Demyk et al. 2022). Samples labelled 'E' consist of submicron-sized particles with irregular shapes that are characterised by prolates with axial ratios of $a/b \sim 2$ and glassy silicate with $a/b \sim 1.5$. These axial ratios are used in the following.

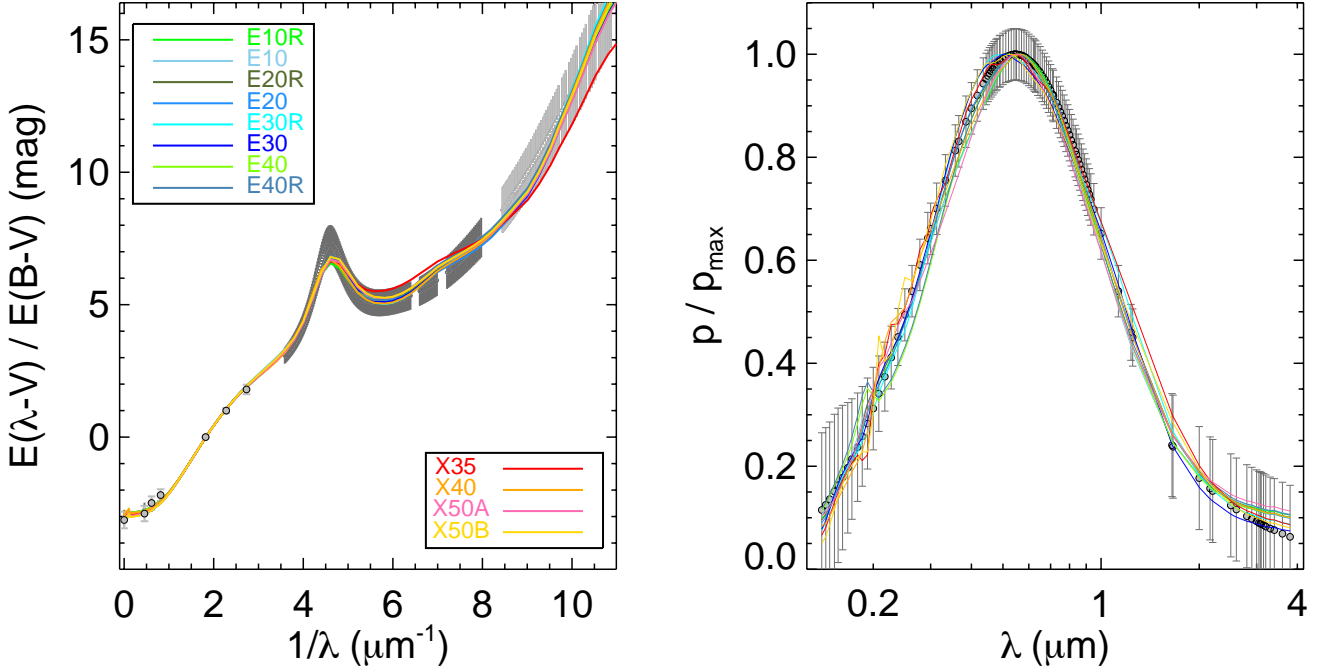
The fitting procedure of Sect. 4.2 is applied to the dust models by replacing the optical constants of the large silicate grains with those by Demyk et al. (2022) measured at 10 K. The alignment efficiency of silicates is set to $\delta_0 = 1 \mu\text{m}$. First, the contribution of dark dust is neglected. The models that are consistent with the abundance constraints (Eq. 1) and that best fit the reddening and starlight polarisation and the emission of po-

⁵ <https://www2.mpia-hd.mpg.de/HJPDO>

Table 2. Parameters of the dust model for the diffuse ISM using Demyk et al. (2022) optical constants for amorphous silicate grains.

1	2	3	4	5	6	7	8	9	10	11	12	13	14	15	16	17	18
Sample				Abundances [†] $\frac{[X]}{[H]}$				Sizes					Derived quantities [‡]				
ID	Composition	μ (u)	ρ (g/cm ³)	vSi	aC	VSG (ppm)	PAH	q	r_{Si}^+	r_{ac}^+	$r_{pol,Si}^-$ (nm)	$r_{pol,aC}^-$	χ^2	$\frac{[C]}{[Si]}$	$\frac{M_{gas}}{M_{dust}}$	R_V	τ_V
X35	0.65 MgO–0.35 SiO ₂	141	2.7	3	72	11	9	3.2	261	262	92	222	1.7	5.0	< 115	–	–
X40	0.60 MgO–0.40 SiO ₂	121	2.7	4	29	7	8	2.9	286	261	72	88	0.5	2.4	< 168	2.94	–
X50A	0.50 MgO–0.50 SiO ₂	100	2.7	3	57	10	6	3.0	267	248	54	72	0.8	4.0	< 129	3.10	1.04
X50B	0.50 MgO–0.50 SiO ₂	100	2.7	4	63	11	7	3.0	257	251	102	233	0.8	4.3	< 162	3.14	–
E10	Mg _{0.9} Fe _{0.1} ³⁺ SiO ₃	99.9	2.8	5	77	12	8	2.9	246	230	59	84	0.7	4.8	< 148	3.08	–
E20	Mg _{0.8} Fe _{0.2} ³⁺ SiO ₃	99.3	2.9	3	41	10	6	3.0	266	253	72	97	0.7	3.1	< 141	3.09	–
E30	Mg _{0.7} Fe _{0.3} ³⁺ SiO ₃	99.8	3.0	5	76	13	9	3.1	259	227	84	183	0.5	4.9	< 165	2.99	–
E40	Mg _{0.6} Fe _{0.4} ³⁺ SiO ₃	99.3	3.1	5	75	12	9	3.1	235	252	57	92	0.6	4.9	< 161	3.05	1.15
E10R	Mg _{0.9} Fe _{0.1} ²⁺ SiO ₃	99.9	2.8	4	64	10	8	3.0	257	238	66	92	0.7	4.2	< 159	3.05	–
E20R	Mg _{0.8} Fe _{0.2} ²⁺ SiO ₃	99.3	2.9	3	46	9	6	3.0	267	260	69	92	0.7	3.3	< 160	3.11	–
E30R	Mg _{0.7} Fe _{0.3} ²⁺ SiO ₃	99.8	3.0	6	85	13	10	3.0	235	234	88	192	0.5	5.2	< 159	3.00	1.18
E40R	Mg _{0.6} Fe _{0.4} ²⁺ SiO ₃	99.3	3.1	5	73	13	8	3.2	237	244	59	102	0.6	4.8	< 162	2.98	1.14

Notes. Notation as in Table 1. [†] Abundance of large amorphous silicate grains are $[Si]/[H] = 15$ ppm. [‡] Models that do not fit the reddening or polarised emission (Planck Collaboration et al. 2020) are indicated by symbol ‘–’ and models that do not fit the dust emission (Dwek et al. 1997; Planck Collaboration et al. 2015) are indicated by symbol ‘<’.


Fig. 9. Best fits (full line) to the reddening (left) and starlight polarisation (right) using Demyk et al. (2022) optical constants as labelled. Model parameters as in Table 2 and data as in Fig. 1 and Fig. 3, respectively.

larised and unpolarised light simultaneously are shown in Fig. 9 - Fig. 11. Sample characteristics, dust parameters, and derived quantities of these models are summarised in Table 2. In that table, columns 1 - 4 provide the identifier, composition, molecular weight μ of the mean composition, and bulk density ρ of the sample as given by Demyk et al. (2022). Parameters for the abundances of the dust populations (columns 4 - 8) and their size parameters (columns 9 - 13) are specified. The derived quantities such as the dust abundance ratio (col. 15), the dust-to-gas mass ratio (col. 16), the total-to-selective extinction (col. 17), and the optical depth (col. 18) that match the optical-to-submm polariza-

tion ratio of $p_{850\mu m}/(p_V/\tau_V) = 4.31$ (Eq. 8) by Planck Collaboration et al. (2020). The goodness parameter of the fit is given in col. 14.

The mean reddening curve is fit by all samples reasonably well except for sample X35, which overestimates the reddening between 5 - 7 (μm^{-1}) and underestimates the far UV rise (Fig. 9, left). The starlight polarisation spectrum is fit within the errors by all models (Fig. 9, right), although at somewhat larger dispersion than the dark dust model shown in Fig. 3.

However, none of these models fit the dust emission (Fig. 10). All models except sample X35 underestimate the FIR

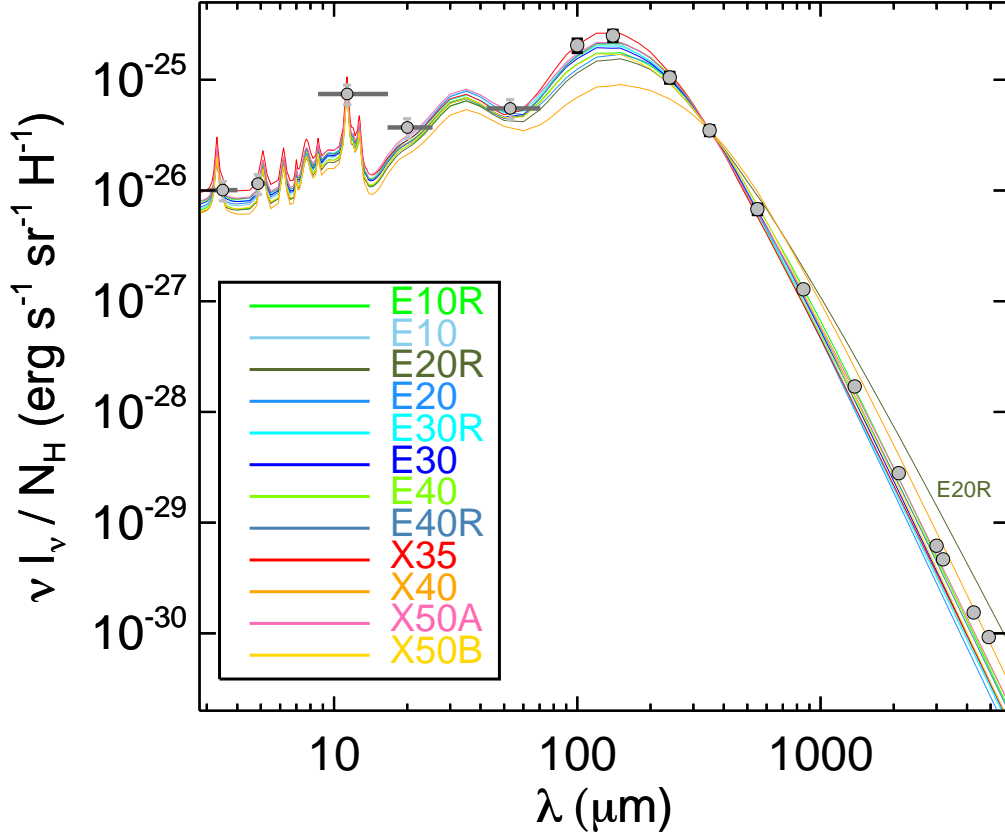


Fig. 10. Dust emission of the diffuse ISM for models using Demyk et al. (2022) optical constants (as labelled) that fit simultaneously the reddening and starlight polarization (Fig. 9). Model parameters as in Table 2 and data as in Fig. 2.

and all models except samples E20R and X50B underestimate the emission > 0.5 mm (Fig. 10). Thus estimates of the dust-to-gas mass ratios for these models shall be taken with caution. The model features of the dust emission become more apparent in the left panel of Fig. 11, where the ratio of the flux to the observed photometry is shown. Samples that do not fit the observed polarised emission spectrum are indicated by a dashed line and those that do are shown by full lines, those are samples E30R, E40R, E40 and X40. The potpourri of the fits to the polarised emission spectrum is shown in the right panel of Fig. 11. Samples that do not fit the $0.25 - 0.5$ mm polarisation spectrum by Gandilo et al. (2016), Shariff et al. (2019), and Ashton et al. (2018) within 15% or deviates by more than 5σ from the Planck Collaboration et al. (2020) polarisation spectrum in the millimetre are indicated by dashed lines.

Mixing the curves that are shown in the panels of Fig. 11 allows finding a flattened curve that better fits the data. The sample X50A appears particularly attractive as it fits the polarization data and the FIR/submm emission up to 0.8 mm already. That model only falls short in the mm-region and this deficit emission may be filled-up using sample E20R that gravely overestimates the submm/mm emission. Indeed a 97:3 mix in mass of the $\text{MgO}-0.5 \text{ SiO}_2$ (X50A) and $\text{Mg}_{0.8}\text{Fe}_{0.2}^{2+} \text{ SiO}_3$ (E20R) provides a simultaneous fit to all the observing constraints. This dust mix without a contribution by dark dust is shown in Fig. 12 together with models that include dark dust contributing to 5% and 10% to the total dust mass, respectively. The best fit using Draine (2003) optical constants and parameters as in Table 1 for

the $r_{\text{Dark}}^+ = 1 \mu\text{m}$ model is shown for comparison. All four models provide a similarly good fit to the data.

7. Conclusion

Dark dust was suggested for the unification of spectroscopic and parallax-derived distances. Such grains have a wavelength-independent reddening and non-selective extinction in the optical were already considered by Trumpler (1930). The extinction properties of these particles require that they are large. Their absorbed energy will be re-emitted in the FIR-mm.

In this paper dark dust has been included as an additional grain population. The model copes with the current state of observations and provides constraints on the physical properties of dust in the diffuse ISM. Major observations that have been verified are representative solid-phase element abundances, far UV-NIR reddening, optical-NIR polarized extinction, FIR-mm dust emission of polarized and unpolarized light, and the ratio of the optical-to-submm polarization. A dust model with 11 parameters for the various grain abundances, sizes, and alignment properties accounts for these data simultaneously. The parameter space is explored by a vectorised iterative fitting procedure to derive the physical properties of dark dust. Different sets of optical constants for amorphous silicate grains are analysed. The principal findings of that study are:

1. A large set of models that account for the mean reddening, extinction and starlight polarization curves of the Milky Way fail to respect the adopted abundance constraints.

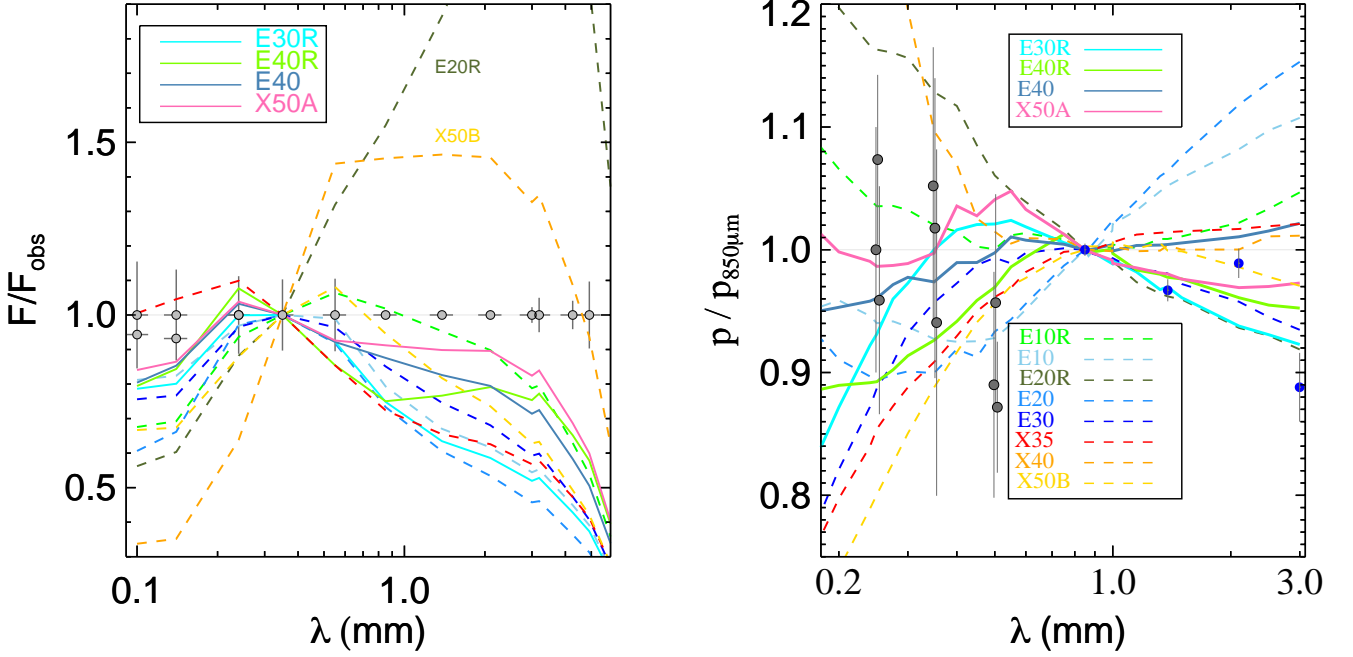


Fig. 11. Flux ratio to the observed photometry (left) and the polarised emission spectrum (right) with data as in Fig. 2 and Fig. 8, respectively. Models using Demyk et al. (2022) optical constants (as labelled) that do not fit the polarised emission spectrum are shown by dashed lines otherwise by a full line.

2. A detailed fit to the Serkowski curve is derived assuming different alignment characteristics of large aC and Si grains.
3. Dark dust consists of micrometre-sized particles of at least $r_{\text{Dark}}^+ \gtrsim 1 \mu\text{m}$.
4. Dark dust provides a significant wavelength-independent reddening in the UV/optical and up to wavelengths $\lambda \lesssim r_{\text{Dark}}^+$.
5. In the FIR/mm the extinction cross-section of dark dust is of similar strengths than Si grains and shows a slightly less steep slope than large grains.
6. The detected Planck excess emission at $0.8 - 3 \text{ mm}$ that previous models cannot explain without ad-hoc changes in the slope of the dust emissivity or adjustments of the optical constants is provided by the emission of very cold ($8 - 12 \text{ K}$) dark dust. Very cold dust is frequently observed in other non-active galaxies.
7. The observed flatness of the submm/mm polarization spectrum is held by the model unless the mass in dark dust is $\lesssim 12 \%$ of the total dust mass.
8. Dark dust, when treated as aligned prolate particles with $r_{\text{Dark}}^+ = 1 \mu\text{m}$, does not provide a significant contribution to the observed polarized extinction, polarization in the $10 \mu\text{m}$ silicate band, and polarized emission at $\lambda \lesssim 1 \text{ mm}$. At longer wavelengths ($1 - 3 \text{ mm}$) dark dust may contribute to $\sim 1/3$ of the maximum polarization.
9. Dark dust models fit the characteristic value of the optical-to-submm polarization ratio assuming an optical depth of $\tau_V = 1.25 \pm 0.13$. The total-to-selective extinction varies between $2.9 \lesssim R_V \lesssim 3.2$, which translates to a mean reddening of $E(B - V) \sim 0.4 \text{ mag}$.
10. The gas-to-dust mass ratio of $M_{\text{gas}}/M_{\text{dust}} = 126 \pm 4$ in the models using optical constants by Draine (2003). The esti-

mate is consistent when using a 97:3 mix in mass of silicate dust analogous to the samples by Demyk et al. (2022) of $\text{MgO}-0.5 \text{ SiO}_2$ and $\text{Mg}_{0.8}\text{Fe}_{0.2}^{2+}$. The later mixture provides a good fit to the observing constraints and still accommodates up to 5 - 10% of mass in dark dust.

Present spectro-polarization in the MIR demonstrates the ability to constrain the stoichiometry of silicate grains. More sensitive MIR polarization spectra are required along sightlines of the diffuse ISM to constrain the models presented here. Dark dust with icy grain mantles would foster grain growth and provide a reservoir for the yet unaccounted O depletion. For the manifestation of such a model ice absorption features in the diffuse ISM need to be detected. Observations shall be possible utilizing the high sensitivity of the JWST spectrometers.

The dark dust model will be applied to individual sightlines to explain the absolute reddening and polarization towards selected stars. This requires a unification of distance estimates to the star either when derived by spectroscopy or from parallax. Dust models that ignore dark dust do not account for the unification of both distance estimates. Dark dust causes significant dimming of light that is not treated in some contemporary research for example by estimating spectroscopic distances and the calibration of SN Ia light curves (Phillips 1993; Riess et al. 1996). This deserves further investigation.

Acknowledgements. I am grateful to Karen Demyk for granting me early access to optical constants of the laboratory samples of amorphous silicate grains. I am grateful to Endrik Krügel and Rolf Chini for helpful discussions.

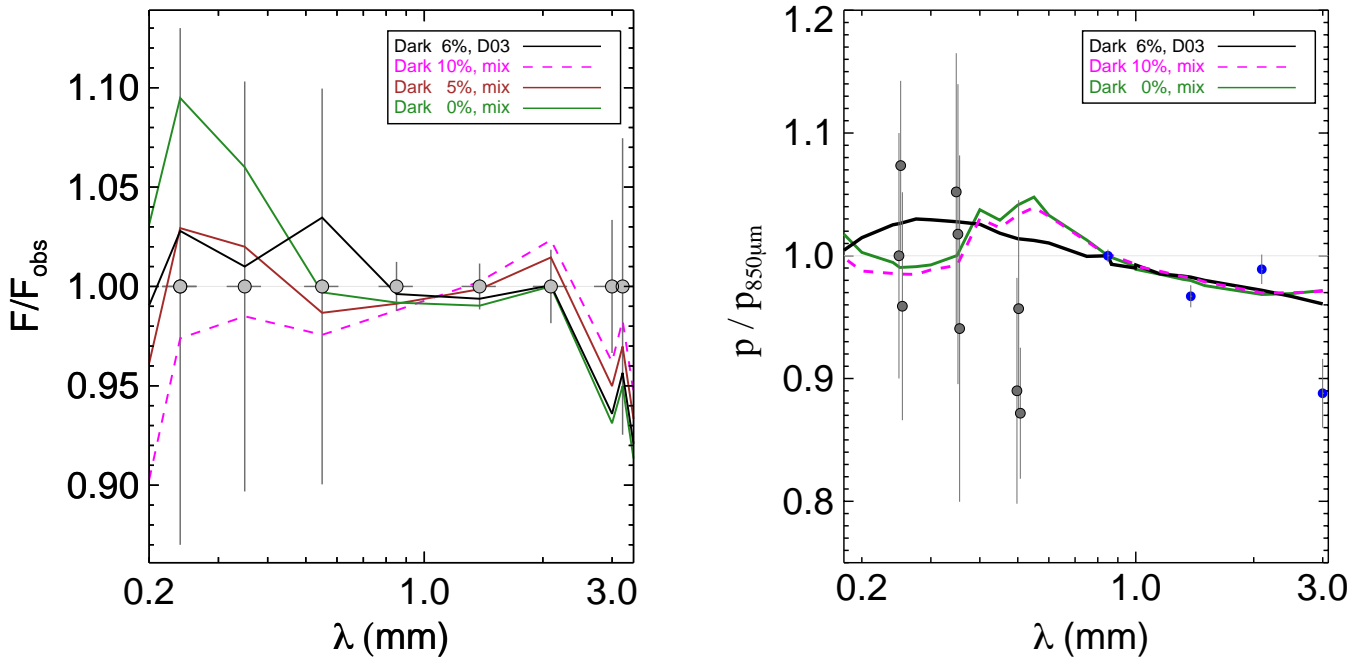


Fig. 12. As Fig. 11 for a 97:3 mix in mass of the $\text{MgO}-0.5 \text{ SiO}_2$ (X50A) and $\text{Mg}_{0.8}\text{Fe}_{0.2}^+ \text{ SiO}_3$ (E20R) Demyk et al. (2022) samples. This model with a contribution to the total dust mass of 0 (green), 5% (brown), and 10% (magenta) of dark dust is shown. The best fit using Draine (2003) optical constants and parameters as in Table 1 for the $r_{\text{Dark}}^+ = 1 \mu\text{m}$ model (black) is shown for comparison.

References

- Allamandola, L. J., Tielens, A. G. G. M., & Barker, J. R. 1989, *ApJS*, 71, 733
 Andersson, B. G., Lazarian, A., & Vaillancourt, J. E. 2015, *ARA&A*, 53, 501
 Andriesse, C. D., Donn, B. D., & Viotti, R. 1978, *MNRAS*, 185, 771
 Ashton, P. C., Ade, P. A. R., Angilè, F. E., et al. 2018, *ApJ*, 857, 10
 Asplund, M., Grevesse, N., Sauval, A. J., & Scott, P. 2009, *ARA&A*, 47, 481
 Bagnulo, S., Cox, N. L. J., Cikota, A., et al. 2017, *A&A*, 608, A146
 Bailer-Jones, C. A. L., Rybizki, J., Founesneau, M., Demleitner, M., & Andrae, R. 2021, *AJ*, 161, 147
 Bailer-Jones, C. A. L., Rybizki, J., Founesneau, M., Mantelet, G., & Andrae, R. 2018, *AJ*, 156, 58
 Blum, J. & Wurm, G. 2008, *ARA&A*, 46, 21
 Bohlin, R. C., Savage, B. D., & Drake, J. F. 1978, *ApJ*, 224, 132
 Bohren, C. F. & Huffman, D. R. 1983, *Absorption and scattering of light by small particles* (ISBN)
 Bowen, D. V., Jenkins, E. B., Tripp, T. M., et al. 2008, *ApJS*, 176, 59
 Chen, X., Wang, S., Deng, L., & de Grijis, R. 2018, *ApJ*, 859, 137
 Chini, R., Hoffmeister, V. H., Nasser, A., Stahl, O., & Zinnecker, H. 2012, *MNRAS*, 424, 1925
 Chini, R., Krügel, E., Haslam, C. G. T., et al. 1993, *A&A*, 272, L5
 Compiègne, M., Verstraete, L., Jones, A., et al. 2011, *A&A*, 525, A103
 Das, H. K., Voshchinnikov, N. V., & Il'in, V. B. 2010, *MNRAS*, 404, 265
 Demyk, K., Gromov, V., Meny, C., et al. 2022, *arXiv e-prints*, arXiv:2209.06513
 Demyk, K., Meny, C., Leroux, H., et al. 2017a, *A&A*, 606, A50
 Demyk, K., Meny, C., Lu, X. H., et al. 2017b, *A&A*, 600, A123
 Deng, D., Sun, Y., Wang, T., Wang, Y., & Jiang, B. 2022, *ApJ*, 935, 175
 Desert, F. X., Boulanger, F., & Puget, J. L. 1990, *A&A*, 500, 313
 Do-Duy, T., Wright, C. M., Fujiyoshi, T., et al. 2020, *MNRAS*, 493, 4463
 Dorschner, J., Begemann, B., Henning, T., Jaeger, C., & Mutschke, H. 1995, *A&A*, 300, 503
 Draine, B. T. 2003, *ApJ*, 598, 1017
 Draine, B. T. & Flatau, P. J. 1994, *Journal of the Optical Society of America A*, 11, 1491
 Draine, B. T. & Friauf, A. A. 2009, *ApJ*, 696, 1
 Draine, B. T. & Hensley, B. S. 2021a, *ApJ*, 909, 94
 Draine, B. T. & Hensley, B. S. 2021b, *ApJ*, 919, 65
 Draine, B. T. & Lee, H. M. 1984, *ApJ*, 285, 89
 Dunkin, S. K. & Crawford, I. A. 1998, *MNRAS*, 298, 275
 Dwek, E., Arendt, R. G., Fixsen, D. J., et al. 1997, *ApJ*, 475, 565
 Dyck, H. M. & Beichman, C. A. 1974, *ApJ*, 194, 57
 Efimov, Y. S. 2009, *Bulletin Crimean Astrophysical Observatory*, 105, 82
 Fanciullo, L., Guillet, V., Aniano, G., et al. 2015, *A&A*, 580, A136
 Fanciullo, L., Kemper, F., Scicluna, P., Dharmawardena, T. E., & Srinivasan, S. 2020, *MNRAS*, 499, 4666
 Fischera, J. 2004, *A&A*, 428, 99
 Fitzpatrick, E. L. & Massa, D. 2007, *ApJ*, 663, 320
 Fitzpatrick, E. L., Massa, D., Gordon, K. D., Bohlin, R., & Clayton, G. C. 2019, *ApJ*, 886, 108
 Gaia Collaboration, Brown, A. G. A., Vallenari, A., et al. 2018, *A&A*, 616, A1
 Gaia Collaboration, Brown, A. G. A., Vallenari, A., et al. 2020, *arXiv e-prints*, arXiv:2012.01533
 Gaia Collaboration, Prusti, T., de Bruijne, J. H. J., et al. 2016, *A&A*, 595, A1
 Galametz, M., Albrecht, M., Kennicutt, R., et al. 2014, *MNRAS*, 439, 2542
 Galametz, M., Madden, S., Galliano, F., et al. 2009, *A&A*, 508, 645
 Galliano, F., Madden, S. C., Jones, A. P., Wilson, C. D., & Bernard, J. P. 2005, *A&A*, 434, 867
 Gandilo, N. N., Ade, P. A. R., Angilè, F. E., et al. 2016, *ApJ*, 824, 84
 Gordon, K. D., Cartledge, S., & Clayton, G. C. 2009, *ApJ*, 705, 1320
 Greenberg, J. M., Li, A., Mendoza-Gomez, C. X., et al. 1995, *ApJ*, 455, L177
 Grenier, I. A., Casandjian, J.-M., & Terrier, R. 2005, *Science*, 307, 1292
 Guillet, V., Fanciullo, L., Verstraete, L., et al. 2018, *A&A*, 610, A16
 Hage, J. I. & Greenberg, J. M. 1990, *ApJ*, 361, 251
 Heinz, S., Corrales, L., Smith, R., et al. 2016, *ApJ*, 825, 15
 Henning, T. 2010, *Annual Review of Astronomy and Astrophysics*, 48, 21
 Hensley, B. S. & Draine, B. T. 2021, *ApJ*, 906, 73
 Herbst, E. 2001, in *Spectroscopy from Space*, ed. J. Demaison, K. Sarka, & E. A. Cohen, 1
 Hong, S. S. & Greenberg, J. M. 1980, *A&A*, 88, 194
 Huffman, D. R. & Stapp, J. L. 1973, in *Interstellar Dust and Related Topics*, ed. J. M. Greenberg & H. C. van de Hulst, Vol. 52, 297
 Indebetouw, R., Mathis, J. S., Babler, B. L., et al. 2005, *ApJ*, 619, 931
 Jäger, C., Dorschner, J., Mutschke, H., Posch, T., & Henning, T. 2003, *A&A*, 408, 193

- Jäger, C., Potapov, A., Rouillé, G., & Henning, T. 2020, in *Laboratory Astrophysics: From Observations to Interpretation*, ed. F. Salama & H. Linnartz, Vol. 350, 27–34
- Jenkins, E. B. 2009, *ApJ*, 700, 1299
- Jones, A. P. 2021, arXiv e-prints, arXiv:2111.04516
- Jones, A. P., Fanciullo, L., Köhler, M., et al. 2013, *A&A*, 558, A62
- Jones, A. P., Köhler, M., Ysard, N., Bocchio, M., & Verstraete, L. 2017, *A&A*, 602, A46
- Jones, A. P., Tielens, A. G. G. M., Hollenbach, D. J., & McKee, C. F. 1994, *ApJ*, 433, 797
- Jones, B. F. 1972, *ApJ*, 171, L57
- Jura, M., Webb, R. A., & Kahane, C. 2001, *ApJ*, 550, L71
- Kataoka, A., Tsukagoshi, T., Pohl, A., et al. 2017, *ApJ*, 844, L5
- Kennicutt, R. C., Calzetti, D., Aniano, G., et al. 2011, *PASP*, 123, 1347
- Knapp, G. R. & Kerr, F. J. 1974, *A&A*, 35, 361
- Köhler, M., Ysard, N., & Jones, A. P. 2015, *A&A*, 579, A15
- Krelowski, J., Galazutdinov, G. A., Strobels, A., & Mulas, G. 2016, *Acta Astron.*, 66, 469
- Krügel, E. 2003, *The physics of interstellar dust (IOP)*
- Krügel, E. 2008, *An introduction to the physics of interstellar dust (IOP)*
- Krügel, E. & Siebenmorgen, R. 1994, *A&A*, 288, 929
- Krügel, E., Siebenmorgen, R., Zota, V., & Chini, R. 1998, *A&A*, 331, L9
- Krüger, H., Strub, P., Grün, E., & Sterken, V. J. 2015, *ApJ*, 812, 139
- Landgraf, M., Baggaley, W. J., Grün, E., Krüger, H., & Linkert, G. 2000, *J. Geophys. Res.*, 105, 10343
- Lanz, T., Heap, S. R., & Hubeny, I. 1995, *ApJ*, 447, L41
- Lenz, D., Hensley, B. S., & Doré, O. 2017, *ApJ*, 846, 38
- Liszt, H. 2014, *ApJ*, 780, 10
- Madden, S. C., Rémy-Ruyer, A., Galametz, M., et al. 2013, *PASP*, 125, 600
- Maercker, M., Khouri, T., Mecina, M., & De Beck, E. 2022, *A&A*, 663, A64
- Maíz Apellániz, J. & Barbá, R. H. 2018, *A&A*, 613, A9
- Maíz-Apellániz, J., Walborn, N. R., Galué, H. Á., & Wei, L. H. 2004, *ApJS*, 151, 103
- Marchenko, S. V. & Moffat, A. F. J. 2017, *MNRAS*, 468, 2416
- Markova, N., Puls, J., Scuderi, S., Simón-Díaz, S., & Herrero, A. 2011, *A&A*, 530, A11
- Markwardt, C. B. 2009, in *Astronomical Society of the Pacific Conference Series*, Vol. 411, *Astronomical Data Analysis Software and Systems XVIII*, ed. D. A. Bohlender, D. Durand, & P. Dowler, 251
- Martin, P. G., Adamson, A. J., Whittet, D. C. B., et al. 1992, *ApJ*, 392, 691
- Martins, F. 2018, *A&A*, 616, A135
- Mathis, J. S., Mezger, P. G., & Panagia, N. 1983, *A&A*, 500, 259
- Mathis, J. S., Rimpl, W., & Nordsieck, K. H. 1977, *ApJ*, 217, 425
- Mathis, J. S. & Whiffen, G. 1989, *ApJ*, 341, 808
- Mennella, V., Baratta, G. A., Esposito, A., Ferini, G., & Pendleton, Y. J. 2003, *ApJ*, 587, 727
- Mennella, V., Brucato, J. R., Colangeli, L., et al. 1998, *ApJ*, 496, 1058
- Mirabel, I. F. & Gergely, T. E. 1979, *A&A*, 77, 110
- Mishchenko, M. I. 2000, *Appl. Opt.*, 39, 1026
- Muñoz, O., Moreno, F., Gómez-Martín, J. C., et al. 2020, *ApJS*, 247, 19
- Mulas, G., Zonca, A., Casu, S., & Cecchi-Pestellini, C. 2013, *ApJS*, 207, 7
- Nguyen, H., Dawson, J. R., Miville-Deschênes, M. A., et al. 2018, *ApJ*, 862, 49
- Nieva, M. F. & Przybilla, N. 2012, *A&A*, 539, A143
- Ossenkopf, V. 1991, *A&A*, 251, 210
- Pecaut, M. J. & Mamajek, E. E. 2013, *ApJS*, 208, 9
- Phillips, M. M. 1993, *ApJ*, 413, L105
- Planck Collaboration, Abergel, A., Ade, P. A. R., et al. 2014, *A&A*, 566, A55
- Planck Collaboration, Ade, P. A. R., Aghanim, N., et al. 2015, *A&A*, 576, A106
- Planck Collaboration, Aghanim, N., Akrami, Y., et al. 2020, *A&A*, 641, A12
- Potapov, A., Bouwman, J., Jäger, C., & Henning, T. 2021, *Nature Astronomy*, 5, 78
- Rachford, B. L., Snow, T. P., Destree, J. D., et al. 2009, *ApJS*, 180, 125
- Rémy-Ruyer, A., Madden, S. C., Galliano, F., et al. 2013a, *A&A*, 557, A95
- Rémy-Ruyer, A., Madden, S. C., Galliano, F., et al. 2013b, *A&A*, 557, A95
- Riess, A. G., Press, W. H., & Kirshner, R. P. 1996, *ApJ*, 473, 88
- Salama, F., Bakes, E. L. O., Allamandola, L. J., & Tielens, A. G. G. M. 1996, *ApJ*, 458, 621
- Scicluna, P., Kemper, F., McDonald, I., et al. 2022, *MNRAS*, 512, 1091
- Scicluna, P., Siebenmorgen, R., Wesson, R., et al. 2015, *A&A*, 584, L10
- Scott, A. & Duley, W. W. 1996, *ApJS*, 105, 401
- Serkowski, K., Mathewson, D. S., & Ford, V. L. 1975, *ApJ*, 196, 261
- Shariff, J. A., Ade, P. A. R., Angilè, F. E., et al. 2019, *ApJ*, 872, 197
- Shull, J. M. & Danforth, C. W. 2019, *ApJ*, 882, 180
- Siebenmorgen, R. & Gredel, R. 1997, *ApJ*, 485, 203
- Siebenmorgen, R., Krelowski, J., Smoker, J., Galazutdinov, G., & Bagnulo, S. 2020, *A&A*, 641, A35
- Siebenmorgen, R., Krügel, E., & Chini, R. 1999, *A&A*, 351, 495
- Siebenmorgen, R., Scicluna, P., & Krelowski, J. 2018a, *A&A*, 620, A32
- Siebenmorgen, R., Voshchinnikov, N. V., & Bagnulo, S. 2014, *A&A*, 561, A82
- Siebenmorgen, R., Voshchinnikov, N. V., Bagnulo, S., et al. 2018b, *A&A*, 611, A5
- Skórzyński, W., Strobels, A., & Galazutdinov, G. A. 2003, *A&A*, 408, 297
- Smith, C. H., Wright, C. M., Aitken, D. K., Roche, P. F., & Hough, J. H. 2000, *MNRAS*, 312, 327
- Sofia, U. J. & Meyer, D. M. 2001, *ApJ*, 558, L147
- Sota, A., Maíz Apellániz, J., Morrell, N. I., et al. 2014, *ApJS*, 211, 10
- Sota, A., Maíz Apellániz, J., Walborn, N. R., et al. 2011, *ApJS*, 193, 24
- Stecher, T. P. 1965, *ApJ*, 142, 1683
- Steinacker, J., Andersen, M., Thi, W. F., et al. 2015, *A&A*, 582, A70
- Strom, K. M., Strom, S. E., & Yost, J. 1971, *ApJ*, 165, 479
- Trumpler, R. J. 1930, *PASP*, 42, 214
- Valencic, L. A., Clayton, G. C., & Gordon, K. D. 2004, *ApJ*, 616, 912
- Voshchinnikov, N. V. 2004, *Astrophys. Space Phys. Res.*, 12, 1
- Voshchinnikov, N. V. 2012, *J. Quant. Spectr. Rad. Transf.*, 113, 2334
- Voshchinnikov, N. V. & Farafonov, V. G. 1993, *Ap&SS*, 204, 19
- Voshchinnikov, N. V. & Henning, T. 2010, *A&A*, 517, A45
- Voshchinnikov, N. V., Henning, T., Prokopenko, M. S., & Das, H. K. 2012, *A&A*, 541, A52
- Voshchinnikov, N. V., Il'in, V. B., & Das, H. K. 2016, *MNRAS*, 462, 2343
- Walborn, N. R. 1971, *ApJS*, 23, 257
- Walborn, N. R. & Fitzpatrick, E. L. 1990, *PASP*, 102, 379
- Wang, S. & Chen, X. 2019, *ApJ*, 877, 116
- Weingartner, J. C. & Draine, B. T. 2001, *ApJ*, 548, 296
- Westphal, A. J., Stroud, R. M., Bechtel, H. A., et al. 2014, *Science*, 345, 786
- Whittet, D. C. B., Martin, P. G., Hough, J. H., et al. 1992, *ApJ*, 386, 562
- Widmark, A., Korsmeier, M., & Linden, T. 2022, arXiv e-prints, arXiv:2208.11704
- Wilking, B. A., Lebofsky, M. J., Martin, P. G., Rieke, G. H., & Kemp, J. C. 1980, *ApJ*, 235, 905
- Witt, A. N., Smith, R. K., & Dwek, E. 2001, *ApJ*, 550, L201
- Wright, C. M., Aitken, D. K., Smith, C. H., Roche, P. F., & Laureijs, R. J. 2002, in *The Origin of Stars and Planets: The VLT View*, ed. J. F. Alves & M. J. McCaughrean, 85
- Wurm, G. & Blum, J. 1998, *Icarus*, 132, 125
- Wurm, G. & Teiser, J. 2021, *Nature Reviews Physics*, 3, 405
- Ysard, N. 2020, in *Laboratory Astrophysics: From Observations to Interpretation*, ed. F. Salama & H. Linnartz, Vol. 350, 53–60
- Ysard, N., Köhler, M., Jones, A., et al. 2015, *A&A*, 577, A110
- Zhu, H., Tian, W., Li, A., & Zhang, M. 2017, *MNRAS*, 471, 3494
- Zhukovska, S., Henning, T., & Dobbs, C. 2018, *ApJ*, 857, 94
- Zubko, V., Dwek, E., & Arendt, R. G. 2004, *ApJS*, 152, 211
- Zubko, V. G., Mennella, V., Colangeli, L., & Bussoletti, E. 1996, *MNRAS*, 282, 1321